Assessing Model Assumptions for Turbulent Premixed Combustion at High Karlovitz Number

Guillaume Blanquart
CALIFORNIA INSTITUTE OF TECHNOLOGY

09/03/2015
Final Report

REPORT DOCUMENTATION PAGE

Form Approved
OMB No. 0704-0188

The public reporting burden for this collection of information is estimated to average 1 hour per response, including the time for reviewing instructions, searching existing data sources, gathering and maintaining the data needed, and completing and reviewing the collection of information. Send comments regarding this burden estimate or any other aspect of this collection of information, including suggestions for reducing the burden, to the Department of Defense, Executive Service Directorate (0704-0188). Respondents should be aware that notwithstanding any other provision of law, no person shall be subject to any penalty for failing to comply with a collection of information if it does not display a currently valid OMB control number.

PLEASE DO NOT RETURN YOUR FORM TO THE ABOVE ORGANIZATION.

1. REPORT DATE *(DD-MM-YYYY)*	2. REPORT TYPE	3. DATES COVERED *(From - To)*
31-08-2015	Final report	01-06-2012 - 31-05-2015

4. TITLE AND SUBTITLE
Assessing Model Assumptions for Turbulent Premixed Combustion at High Karlovitz Number

5a. CONTRACT NUMBER
NA

5b. GRANT NUMBER
FA9550-12-1-0144

5c. PROGRAM ELEMENT NUMBER
NA

6. AUTHOR(S)
Guillaume Blanquart

5d. PROJECT NUMBER
NA

5e. TASK NUMBER
NA

5f. WORK UNIT NUMBER
NA

7. PERFORMING ORGANIZATION NAME(S) AND ADDRESS(ES)
California Institute of Technology
1200 E California Blvd, Pasadena, CA 91125, USA

8. PERFORMING ORGANIZATION REPORT NUMBER
NA

9. SPONSORING/MONITORING AGENCY NAME(S) AND ADDRESS(ES)
Air Force Office of Science and Research
875 Randolph Street
Suite 325 Room 3112
Arlington, VA 22203

10. SPONSOR/MONITOR'S ACRONYM(S)
NA

11. SPONSOR/MONITOR'S REPORT NUMBER(S)
NA

12. DISTRIBUTION/AVAILABILITY STATEMENT
Distribution A - Approved for Public Release

13. SUPPLEMENTARY NOTES

14. ABSTRACT
Premixed turbulent flames in the high-Karlovitz regime are characterized and modeled using Direct Numerical Simulations (DNS) with detailed chemistry. To enable the present numerical study, a new time-integration scheme has been proposed for the simulation of stiff reacting flows. Using this scheme, a series of direct numerical simulations of high Karlovitz number, n-C7H16, turbulent premixed flames have been performed. It was found that the flame structure of these turbulent flames can be well captured by one-dimensional flames accounting for the effective species Lewis numbers. The reaction zone was found to remain thin, yet large fluctuations in the fuel burning rate were identified. Extinctions were observed only in the presence of differential diffusion, and these events were correlated with high curvature regions. A model to capture the burning fluctuations was proposed using a new flamelet approach. For the first time, the evolution of the turbulence (both turbulent kinetic energy and enstrophy) has been characterized through the flame. Under sufficiently high Karlovitz number, the first Kolmogorov's hypothesis has been confirmed. Finally, the impact of various chemical/transport model assumptions on the evolution of turbulent flow field.

15. SUBJECT TERMS
Turbulent premixed flames, heptane, differential diffusion, Direct Numerical Simulations, detailed chemistry

16. SECURITY CLASSIFICATION OF:

a. REPORT	b. ABSTRACT	c. THIS PAGE	17. LIMITATION OF ABSTRACT	18. NUMBER OF PAGES	19a. NAME OF RESPONSIBLE PERSON
U	U	U	UU		Prof./Dr. Guillaume Blanquart

19b. TELEPHONE NUMBER *(Include area code)*
626-395-4306

Reset

Standard Form 298 (Rev. 8/98)
Prescribed by ANSI Std. Z39.18
Adobe Professional 7.0

INSTRUCTIONS FOR COMPLETING SF 298

1. REPORT DATE. Full publication date, including day, month, if available. Must cite at least the year and be Year 2000 compliant, e.g. 30-06-1998; xx-06-1998; xx-xx-1998.

2. REPORT TYPE. State the type of report, such as final, technical, interim, memorandum, master's thesis, progress, quarterly, research, special, group study, etc.

3. DATES COVERED. Indicate the time during which the work was performed and the report was written, e.g., Jun 1997 - Jun 1998; 1-10 Jun 1996; May - Nov 1998; Nov 1998.

4. TITLE. Enter title and subtitle with volume number and part number, if applicable. On classified documents, enter the title classification in parentheses.

5a. CONTRACT NUMBER. Enter all contract numbers as they appear in the report, e.g. F33615-86-C-5169.

5b. GRANT NUMBER. Enter all grant numbers as they appear in the report, e.g. AFOSR-82-1234.

5c. PROGRAM ELEMENT NUMBER. Enter all program element numbers as they appear in the report, e.g. 61101A.

5d. PROJECT NUMBER. Enter all project numbers as they appear in the report, e.g. 1F665702D1257; ILIR.

5e. TASK NUMBER. Enter all task numbers as they appear in the report, e.g. 05; RF0330201; T4112.

5f. WORK UNIT NUMBER. Enter all work unit numbers as they appear in the report, e.g. 001; AFAPL30480105.

6. AUTHOR(S). Enter name(s) of person(s) responsible for writing the report, performing the research, or credited with the content of the report. The form of entry is the last name, first name, middle initial, and additional qualifiers separated by commas, e.g. Smith, Richard, J, Jr.

7. PERFORMING ORGANIZATION NAME(S) AND ADDRESS(ES). Self-explanatory.

8. PERFORMING ORGANIZATION REPORT NUMBER. Enter all unique alphanumeric report numbers assigned by the performing organization, e.g. BRL-1234; AFWL-TR-85-4017-Vol-21-PT-2.

9. SPONSORING/MONITORING AGENCY NAME(S) AND ADDRESS(ES). Enter the name and address of the organization(s) financially responsible for and monitoring the work.

10. SPONSOR/MONITOR'S ACRONYM(S). Enter, if available, e.g. BRL, ARDEC, NADC.

11. SPONSOR/MONITOR'S REPORT NUMBER(S). Enter report number as assigned by the sponsoring/ monitoring agency, if available, e.g. BRL-TR-829; -215.

12. DISTRIBUTION/AVAILABILITY STATEMENT. Use agency-mandated availability statements to indicate the public availability or distribution limitations of the report. If additional limitations/ restrictions or special markings are indicated, follow agency authorization procedures, e.g. RD/FRD, PROPIN, ITAR, etc. Include copyright information.

13. SUPPLEMENTARY NOTES. Enter information not included elsewhere such as: prepared in cooperation with; translation of; report supersedes; old edition number, etc.

14. ABSTRACT. A brief (approximately 200 words) factual summary of the most significant information.

15. SUBJECT TERMS. Key words or phrases identifying major concepts in the report.

16. SECURITY CLASSIFICATION. Enter security classification in accordance with security classification regulations, e.g. U, C, S, etc. If this form contains classified information, stamp classification level on the top and bottom of this page.

17. LIMITATION OF ABSTRACT. This block must be completed to assign a distribution limitation to the abstract. Enter UU (Unclassified Unlimited) or SAR (Same as Report). An entry in this block is necessary if the abstract is to be limited.

Assessing Model Assumptions for Turbulent Premixed Combustion at High Karlovitz Number
Grant Number FA9550-12-1-0144

Guillaume Blanquart

Department of Mechanical Engineering, California Institute of Technology, CA, USA

Abstract

n-heptane/air premixed turbulent flames in the high-Karlovitz portion of the thin reaction zone regime are characterized and modeled using Direct Numerical Simulations (DNS) with detailed chemistry. To enable the present numerical study, a new time-integration scheme has been proposed for the simulation of stiff reacting flows. Using this scheme, a series of direct numerical simulations of high Karlovitz number, n-C_7H_{16}, turbulent premixed flames have been performed. It was found that the flame structure of these turbulent flames can be well captured by one-dimensional flames accounting for the effective species Lewis numbers. The reaction zone was found to remain thin, yet large fluctuations in the fuel burning rate were identified. Extinctions were observed only in the presence of differential diffusion, and these events were correlated with high curvature regions. A model to capture the burning fluctuations was proposed using a new flamelet approach. For the first time, the evolution of the turbulence (both turbulent kinetic energy and enstrophy) has been characterized through the flame. Under sufficiently high Karlovitz number, the first Kolmogorov's hypothesis has been confirmed. Finally, the impact of various chemical/transport model assumptions on the evolution of turbulence has been analyzed.

1. Introduction

1.1. *Regimes of turbulent premixed flames*

Turbulent premixed flames are typically characterized by the extent to which turbulence is "expected" to penetrate/disrupt the flame. The Karlovitz number

$$Ka = \frac{\tau_F}{\tau_\eta}, \tag{1}$$

which is the ratio of the flame time scale $\tau_F = l_F/S_L$ to the Kolmogorov time scale, provides such information [1]. The larger the Karlovitz number, the more turbulence is expected to penetrate/disrupt the flame.

As industrial applications of turbulent premixed (and partially premixed) flames fall in the thin/broken reaction zone regimes, understanding how a flame behaves in these regimes is critical [2]. Experiments are difficult to conduct at high Karlovitz numbers and a limited number of them are available in the literature [3,4]. Equivalently, due to their expensive computational costs, very few Direct Numerical Simulations (DNS) of turbulent premixed flames in the broken reaction zone or the thin reaction zone regimes have been performed [5–10]. Figure 1 presents all of these simulations in the context of the regime diagram (as proposed by Peters [1]). Note that only simulations performed with detailed finite-rate chemistry are presented.

1.2. *Fuel chemistry/transport*

The only fuels that have been considered in previous simulations are hydrogen [5,8], methane [6,7], and propane [6]. While these fuels are used in several ground-based applications [11], most of the fuels used for transportation contain larger hydrocarbons [12,13]. Since their chemical pathways are far more complex, and a wide range of stable species
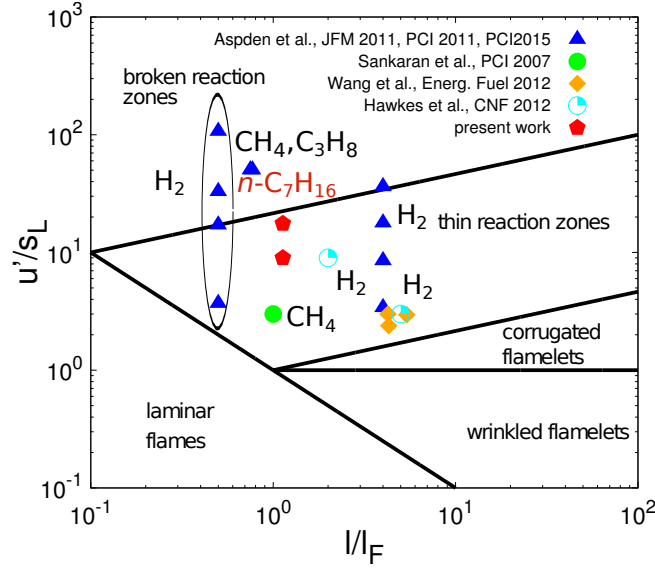
Fig. 1. DNS of high Karlovitz turbulent premixed flames with finite-rate chemistry.

are present through the flame front, it remains unclear how turbulence influences their chemistry at high Karlovitz number.

Moreover, heavy hydrocarbons have large Lewis numbers (*e.g.* $Le_{C_{12}H_{26}} \approx 3.5$). It has also been observed that for sufficiently high Karlovitz number differential diffusion effects were negligible for both H_2 ($Le_{H_2} \approx 0.3$) and C_3H_8 ($Le_{C_3H_8} \approx 2$) [6]. However, this similar behavior between smaller and larger than unity Lewis number fuels cannot be generalized to intermediate Karlovitz numbers as pertinent to the transition between the thin/broken reaction zone regimes. Furthermore, while the series of lean H_2/air premixed flames performed by Aspden *et al.* [5] have provided information on how turbulence affects differential diffusion over a wide range of Karlovitz numbers, there is no such information available for heavy hydrocarbon fuels.

1.3. *Approach*

To tackle these questions, a series of DNS of a premixed n-C_7H_{16} turbulent flames in the thin reaction zone regime and close to the transition between the thin/broken reaction zones regimes are targetted in this work. n-C_7H_{16} is chosen for the fuel because it is used in surrogates for gasoline [14,13]. In addition, it corresponds to a step towards the simulation of n-decane or n-dodecane flames (larger chemical mechanism), which species are often used in surrogates for kerosene [15,16].

More specifically, the following three aspects need to be characterized with these target flames:
  (i) the effect of turbulence on the flame structure and the impact of turbulent mixing on differential diffusion,
 (ii) the effect of turbulence on the reaction zone with and without differential diffusion,
(iii) the effect of the flame on the evolution of the turbulent flow field.

2. Governing equations

2.1. *Fluid mechanics*

The reacting mixture is assumed to contain a total number of N species and their chemistry is assumed to be given by a chemical kinetics mechanism involving K reactions, with forward and backward reactions counted separately. The chemically reacting flows of interest in the current study are of relatively low Mach number (M_a), typically below 0.3 [17,18]. Under this condition, the acoustic waves can be ignored and the pressure field can be decomposed into a spatially-invariant, but (potentially) time-dependent component, $P_0(t)$, and a fluctuating hydrodynamic pressure, $p(\mathbf{x}, t)$ [17–19,1]. Since the focus is on turbulence-chemistry interaction, Soret and Dufour effects, body forces, and radiative heat transfer are ignored [20,21,18,22].

Under these assumptions, the evolution of the system is governed by the following conservation equations of mass, momentum, energy, and species density [23,19,1]:

$$\frac{\partial \rho}{\partial t} + \nabla \cdot (\rho \mathbf{u}) = 0 \tag{2}$$

$$\frac{\partial \rho \mathbf{u}}{\partial t} + \nabla \cdot (\rho \mathbf{u} \otimes \mathbf{u}) = -\nabla p + \nabla \cdot \tau \tag{3}$$

2

$$c_p \left[\frac{\partial \rho T}{\partial t} + \nabla \cdot (\rho \mathbf{u} T) \right] = \nabla \cdot (\rho c_p \alpha \nabla T) + \sum_i c_{p,i} \rho \left(\frac{\alpha}{Le_i} \nabla Y_i + Y_i \mathbf{V_{c,i}} \right) \cdot \nabla T + \dot{\omega}_T \tag{4}$$

$$\frac{\partial \rho Y_i}{\partial t} + \nabla \cdot (\rho \mathbf{u} Y_i) = \nabla \cdot \left(\rho \frac{\alpha}{Le_i} \nabla Y_i \right) + \nabla \cdot (\rho Y_i \mathbf{V_{c,i}}) + \dot{\omega}_i. \tag{5}$$

In the above equations, ρ is the density, $\mathbf{u}$ is the velocity vector, T denotes the temperature of the mixture, and Y_i is the mass fraction of species i. In the momentum equation (Eq. 3), τ is the deviatoric stress tensor, defined as

$$\tau = \mu \left[\nabla \mathbf{u} + (\nabla \mathbf{u})^T \right] - \frac{2}{3} \mu (\nabla \cdot \mathbf{u}) \mathbf{I}, \tag{6}$$

where $\mathbf{I}$ is the identity matrix and μ is the fluid viscosity. In the energy conservation equation (Eq. 4), $\dot{\omega}_T$ includes heat source terms due to chemical reactions, α is the thermal diffusivity, and c_p is the specific heat at constant pressure of the mixture, given by

$$c_p = \sum_{i=1}^{N} Y_i c_{p,i}, \tag{7}$$

where $c_{p,i}$ is the specific heat at constant pressure of species i. In the species conservation equations (Eq. 5), $\dot{\omega}_i$ is the chemical source term of species i, and Le_i is the Lewis number of species i, defined as

$$Le_i = \frac{\alpha}{D_i}, \tag{8}$$

with D_i the mass diffusivity for species i. The correction velocity $\mathbf{V_{c,i}}$ in Eq. 5 accounts for gradients in the mixture molecular weight as well as ensures zero net diffusion flux. It has the following expression [19,1]:

$$\mathbf{V_{c,i}} = \frac{\alpha}{Le_i} \frac{\nabla W}{W} - \alpha \left(\sum_{j=1}^{N} \frac{\nabla Y_j}{Le_j} \right) - \alpha \frac{\nabla W}{W} \left(\sum_{j=1}^{N} \frac{Y_j}{Le_j} \right), \tag{9}$$

where

$$W = \left(\sum_{j=1}^{N} \frac{Y_j}{W_j} \right)^{-1} \tag{10}$$

is the local mean molecular weight of the mixture, and W_j is the molecular weight of species j.

The above set of equations is complemented by the equation of thermodynamic state

$$\rho = \frac{P_0 W}{\widehat{R} T}, \tag{11}$$

where P_0 is the thermodynamic pressure and $\widehat{R}$ is the universal gas constant.

2.2. Chemical model

The overall rate of change of species i, $\dot{\omega}_i$, in Eq. 5 can be split into a production term, $\dot{\omega}_i^+$, and a consumption term, $\dot{\omega}_i^-$, as

$$\dot{\omega}_i = \dot{\omega}_i^+ - \dot{\omega}_i^-. \tag{12}$$

The production rate of species i, $\dot{\omega}_i^+$, is given by the sum of the contributions from all elementary chemical reactions leading to the formation of this species:

$$\dot{\omega}_i^+ = W_i \sum_{\substack{j=1 \\ \nu_{ji}>0}}^{K} \left[k_j \prod_{s=1}^{N} \left(\frac{\rho Y_s}{W_s} \right)^{\nu_{js}} \right], \tag{13}$$

where ν_{js} is the stoichiometric coefficient of species s in reaction j. In the above expression, the rate constant of reaction j, k_j, is given by the Arrhenius form, $k_j(T) = A_j T^{b_j} \exp^{-T_{a,j}/T}$, where $T_{a,j}$ is the activation temperature of this reaction. The consumption rate is writen in a similar manner.

The local heat release rate is given by

$$\dot{\omega}_T = - \sum_{j=1}^{N} h_i \dot{\omega}_i, \tag{14}$$

where

$$h_i = h_i^0 + \int_{T_0}^{T} c_{p,i} dT \tag{15}$$

is the specific enthalpy of species i, and h_i^0 denotes its value under standard and reference conditions.

3. Numerical algorithm

3.1. *Overview of the numerical solver*

The simulations in this work are performed using the structured, multi-physics and multi-scale finite-difference code NGA [17]. The NGA code allows for accurate, robust, and flexible simulations of both laminar and turbulent reactive flows in complex geometries and has been applied in a wide range of test problems, including laminar and turbulent flows [23–25] and constant and variable density flows [17,26,27], as well as Large-Eddy Simulations (LES) [24,28] and Direct Numerical Simulations (DNS) [29,27,30]. This numerical solver has been shown to conserve discretely mass, momentum, and kinetic energy, with arbitrarily high order spatial discretization [17]. NGA uses both spatially and temporally staggered variables [17]. All scalar quantities ($\rho, p, T, Y_i, D_i, \alpha, c_p, c_{p,i}, \mu$) are stored at the volume centers, and the velocity components are stored at their respective volume faces. The convective term in the species transport equations is discretized using the bounded quadratic upwind-biased interpolative convective scheme (BQUICK) [31], and the diffusive term is discretized using a second-order centered scheme. The variables are advanced in time using the second-order semi-implicit Crank-Nicolson scheme of Pierce and Moin [32].

3.2. *Iterative procedure*

An iterative procedure is applied to fully cover the non-linearities in the Navier-Stokes equations. This iterative procedure has been found to be of critical importance for stability and accuracy considerations [17,18,32]. The density, pressure, and scalar fields are advanced from time level $t^{n+1/2}$ to $t^{n+3/2}$, and the velocity fields are advanced from time level t^n to t^{n+1}. The subscript k refers to the sub-iterations.

Traditionally, the scalar fields are advanced in time using the semi-implicit Crank-Nicolson method [17,32] for the convective and diffusive terms, and explicit integration for the chemical source terms:

$$\mathbf{Y}_k^* = \frac{\mathbf{Y}^{n+1/2} + \mathbf{Y}_k^{n+3/2}}{2}, \tag{16}$$

$$\rho_k^{n+3/2} \mathbf{Y}_{k+1}^{n+3/2} = \rho^{n+1/2} \mathbf{Y}^{n+1/2} + \Delta t \left[(\mathbf{C}_k^{n+1} + \mathbf{D}_k^{n+1}) \cdot \mathbf{Y}_k^* + \Omega_k^* \right]$$
$$+ \frac{\Delta t}{2} \left(\frac{\partial \mathbf{C}}{\partial \mathbf{Y}} + \frac{\partial \mathbf{D}}{\partial \mathbf{Y}} \right)_k^{n+1} \cdot \left(\mathbf{Y}_{k+1}^{n+3/2} - \mathbf{Y}_k^{n+3/2} \right). \tag{17}$$

To simplify the discrete notations for spatial differential operators, the operators corresponding to the convective and diffusive terms in the scalar equations (Eq. 5) are written as $\mathbf{C}$ and $\mathbf{D}$, respectively. $\frac{\partial \mathbf{C}}{\partial \mathbf{Y}}$ and $\frac{\partial \mathbf{D}}{\partial \mathbf{Y}}$ are the Jacobian matrices corresponding to the convective and diffusive terms, respectively. For simpler implementation, the set of equations (Eq. 17) is solved in practice in its residual form:

$$\mathbf{Y}_{k+1}^{n+3/2} = \mathbf{Y}_k^{n+3/2} - \Delta t \mathbf{J}^{-1} \cdot \Theta_k, \tag{18}$$

where the matrix $\mathbf{J}$ is defined as

$$\mathbf{J} = \rho_k^{n+3/2} \mathbf{I} - \frac{\Delta t}{2} \left(\frac{\partial \mathbf{C}}{\partial \mathbf{Y}} + \frac{\partial \mathbf{D}}{\partial \mathbf{Y}} \right)_k^{n+1}, \tag{19}$$

and the vector

$$\Theta_k = \frac{\rho_k^{n+3/2} \mathbf{Y}_k^{n+3/2} - \rho^{n+1/2} \mathbf{Y}^{n+1/2}}{\Delta t} - \left[(\mathbf{C}_k^{n+1} + \mathbf{D}_k^{n+1}) \cdot \mathbf{Y}_k^* + \Omega_k^* \right] \tag{20}$$

is the error (residual) made on the species transport equation at the previous sub-iteration. When the sub-iterations are fully-converged, the residual, Θ_k, is zero.

3.3. *Preconditioned iterative method*

The time-marching for species transport equations described in Eq. 18 resembles the standard preconditioned Richardson-type iterative method [33], where the matrix $\mathbf{J}$ acts as a preconditioner. More precisely, the choice of the preconditioner, $\mathbf{J}$, can be arbitrary and does not modify the discrete form of the equations to solve (*i.e.* $\Theta_k = \mathbf{0}$). It only changes the convergence characteristics of the iterative method. For instance, setting

4

$$\mathbf{J} = \rho_k^{n+3/2}\mathbf{I} \tag{21}$$

is equivalent to the fully-explicit integration of the convective, diffusive, and chemical source terms in the species transport equations, while setting

$$\mathbf{J} = \rho_k^{n+3/2}\mathbf{I} - \frac{\Delta t}{2}\left(\frac{\partial \mathbf{C}}{\partial \mathbf{Y}} + \frac{\partial \mathbf{D}}{\partial \mathbf{Y}} + \frac{\partial \Omega}{\partial \mathbf{Y}}\right)_k^{n+1} \tag{22}$$

corresponds to the full-implicit integration of the convective, diffusive, and chemical source terms in the species transport equations.

Clearly, there is a trade-off in the choice of the preconditioner. Since it is applied at each step of the iterative method, it is preferable to have a preconditioning matrix, $\mathbf{J}$, with low computing and inversion cost. The cheapest preconditioner would therefore be the one described by Eq. 21 (fully-explicit integration), which leads to poor convergence performance requiring extremely small time step sizes. On the other hand, the optimal preconditioner would be the one leading to the fully-implicit integration of the various terms (Eq. 22). Unfortunately, since the chemical source terms of most species are generally dependent on a large number of other species, the chemical Jacobian matrix, $\frac{\partial \Omega}{\partial \mathbf{Y}}$, is usually not sparse [34]. Therefore, its construction and inversion may become prohibitively expensive especially when a large number of species is considered.

The proposed preconditioner is written as

$$\mathbf{J} = \rho_k^{n+3/2}\mathbf{I} - \frac{\Delta t}{2}\left(\frac{\partial \mathbf{C}}{\partial \mathbf{Y}} + \frac{\partial \mathbf{D}}{\partial \mathbf{Y}} - \Lambda\right)_k^{n+1}, \tag{23}$$

where Λ is a diagonal matrix defined as

$$\Lambda_{i,i} = \frac{\dot{\omega}_i^-}{Y_i}. \tag{24}$$

The matrix Λ may be regarded as a very good approximation of the diagonal of the chemical Jacobian (see Fig. 2). The proposed preconditioner aims to suppress the small timescales due to the fast consumption of the different species in the system with stiff chemistry.
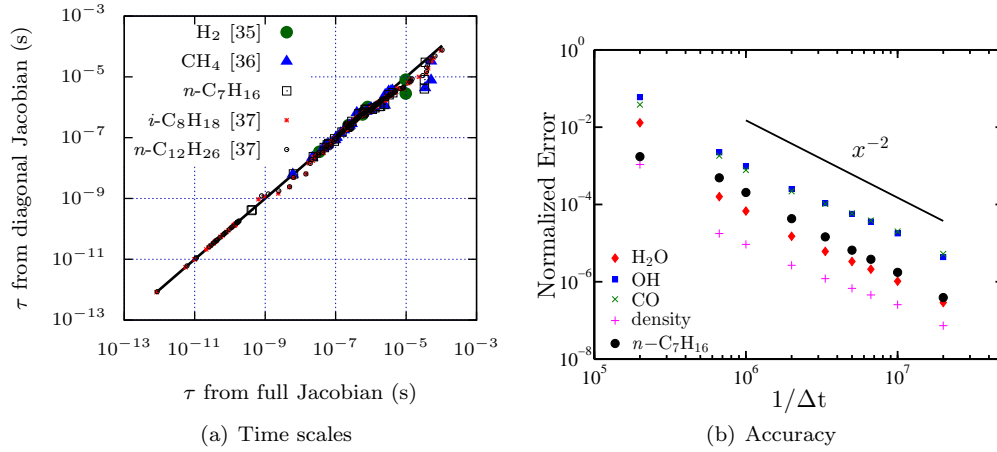

Fig. 2. Comparison of the chemical timescale (τ) of the full chemical Jacobian to the species lifetime of the preconditioned chemical Jacobian at the peak rate of heat release, considering various fuels and chemical mechanisms and temporal accuracy of the method.

3.4. *Scheme performance*

The performance of the proposed method was numerically tested on two flow configurations: a one-dimensional unstretched premixed flame and a three-dimensional turbulent premixed flame, both with an unburnt mixture of air and n-heptane. The method was shown to be second-order accurate in time (Fig. 2). The computational cost of a single iteration with the proposed method is similar to that of an explicit time-integration scheme. Therefore, the simulation speed-up achieved with the proposed method corresponds to the increase in the largest stable time step size. For the three-dimensional turbulent premixed flame, the simulation could be performed with a convective CFL of 0.8 (optimal, with or without chemistry).

The theoretical analysis for stability and convergence rate is general and is not limited by the type of fuel, chemical mechanism, or flow configuration. Therefore, it was repeated, in the context of one-dimensional premixed flames, with several fuels, unburnt conditions, and chemical mechanisms. It was also performed with non-premixed flamelets using different scalar dissipation rates. The method provides good convergence rates of the sub-iterations close to
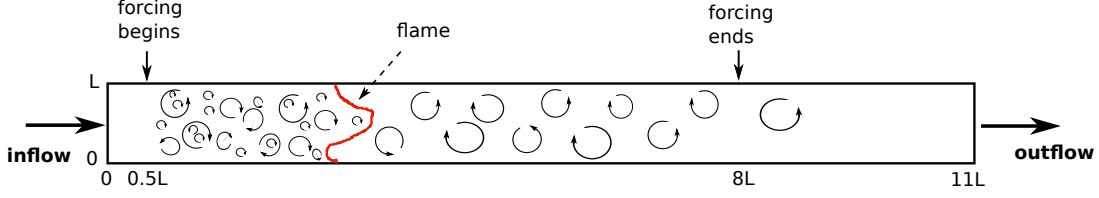
5

Fig. 3. Computational domain demonstrating the approximate location of the flame and region of forcing. Diagram taken from Ref. [38].

	A	B	C	C$'$	D	E
T_u [K]	298	298	800	500	800	298
ρ_u/ρ_b	7.8	7.8	3.3	4.9	3.3	7.8
L_x[mm]	25.6	25.6	16.8	18.7	16.8	25.6
L [mm]	2.33	2.33	1.53	1.70	1.53	2.33
Grid	11×128^3	11×128^3	11×128^3	11×146^3	11×220^3	11×240^3
Re_t	83	190	170	290	380	390
Ka_u	70	220	200	650	750	640
u'/S_L	9	18	19	38	45	37
l_o/l_F	1.1	1.1	1.2	1	1.2	1.1
$\eta_u[\mu m]$	16	9	7	4.6	3.5	5.1
S_L[m/s]	0.36	0.36	2.3	0.86	2.3	0.36
l_F[mm]	0.39	0.39	0.25	0.32	0.25	0.39

Table 1
Physical and numerical parameters of the DNS which employ finite-rate chemistry and non-unity Lewis number transport.

the stability limit for all the chemical mechanisms considered. The proposed preconditioning method showed great potential for the efficient time-integration of turbulent flames. Although not a primary target, the method was also shown to work for a homogeneous ignition case.

Finally, the proposed method is more suited than other methods for reacting flows in which the convective timescales are of the order of 10^{-6} s or less. These correspond to moderately to highly turbulent (non-premixed or premixed) flames (high Karlovitz for premixed flames).

4. Direct Numerical Simulations

4.1. *Physical Configuration*

The present study considers statistically-stationary, statistically-planar premixed turbulent n-heptane/air flames at a slightly lean equivalence ratio ($\phi = 0.9$) and atmospheric pressure. The three-dimensional domain has an inflow and outflow at the left and right x boundaries, respectively, and periodic boundary conditions in the y and z directions (Fig. 3). The height and width of the channel are equal and denoted as L, while the length, L_x, is equal to $11L$. A separate DNS is performed of relatively weak, homogeneous, isotropic, triply periodic box turbulence and is used to generate the inflow condition. The mean inflow velocity is constant for each case and set to a value which approximates the turbulent flame speed, allowing for an arbitrary long run-time. This configuration lacks any mean shear so that the effects of the flame on the turbulence may be specifically studied.

The turbulence and temperature in the reactants are varied between simulations to investigate the effects of both the unburnt Karlovitz number and flame density ratio. All necessary information about the different simulations is provided in Table 1 and 2, where $Re_t = u'l_o/\nu$, u', and η_u are the turbulent Reynolds number, rms velocity fluctuation, and Kolmogorov length scale, respectively, all calculated in the unburnt gas. Cases B_1, $B_{Tab,1}$, $B_{OS,1}$, and $B^4_{Tab,1}$ are performed to test the effects of the transport models, chemical models, and Reynolds number, and use the same method.

Between the cases studied, the unburnt Karlovitz number varies by an order of magnitude (Ka_u=70 - 760) and the unburnt temperature spans all practically relevant conditions (T_u=298 - 800K). Cases A, B, and E have the same density ratio and are used to test the effects of Ka_u independently, while the pairs B, C and E, C$'$ have the same Ka_u and are used to test the density ratio independently. Figure 4 shows Ka_u and the density ratio for each case as well as their location on the Peters' regime diagram. These conditions span the transition from the thin to

6

	B_1	$B_{\text{Tab},1}$	$B_{\text{OS},1}$	$B^4_{\text{Tab},1}$
T_u [K]	298	298	298	298
ρ_u/ρ_b	7.8	7.8	7.3	7.8
L_x[mm]	25.6	25.6	25.6	60.6
L [mm]	2.33	2.33	2.33	9.32
Grid	11×128^3	11×128^3	11×128^3	2574×512^2
Re_t	190	190	190	1150
Ka_u	280	280	250	280
u'/S_L	21	21	22	33
l_o/l_F	1	1	1.2	4
$\eta_u[\mu\text{m}]$	9	9	9	9
S_L[m/s]	0.29	0.29	0.27	0.29
l_F[m]	0.43	0.43	0.36	0.43

Table 2
Physical and numerical parameters of additional DNS which vary the transport and chemical models. Subscripts 1, Tab, and OS correspond to simulations using unity Lewis numbers, tabulated chemistry, and one-step chemistry respectively. Superscript of 4 corresponds to $l_o/l_F = 4$.

(a) Karlovitz numbers and density ratios   (b) Peters regime diagram
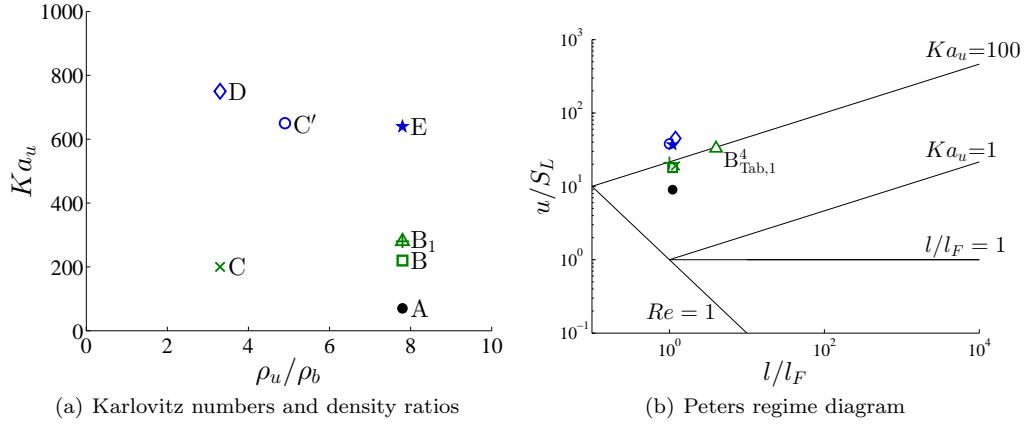
Fig. 4. Conditions in the unburnt flow of performed simulation. Symbols on the left plot correspond to the same simulations on the right.

broken/distributed reaction zone regimes.

Each simulation is run for over 25 eddy turnover times ($\tau_o = k/\epsilon$, where k is the TKE) after an initial transient period, in order to provide sufficient statistical samples. Further specifications of the simulation conditions are listed in Table 1 and 2.

4.2. Turbulence forcing

As all other similarly high Ka numerical simulations from the literature [5,6,39], the present configuration misses the generation of turbulence due to large scale flow straining (larger than the domain size). As a result, the turbulence is expected to decay, and the use of velocity field forcing is necessary.

In previous work, spectral forcing techniques were often used to offset the decay of TKE and maintain the turbulence characteristics [5,39]. In the present work, the linear velocity forcing method [40,41,30] was preferred for its more physical nature and good stability properties [26]. The linearly forced turbulent field under comparable Reynolds number was analyzed in Ref. [30] and it was shown that the second- and third-order structure functions and the energy spectrum are self-consistent and in agreement with experimentally obtained data [42] of decaying grid turbulence. The linear forcing method *mimics* the missing large scale straining by appending a source term to the momentum equation [40,41].

Figure 5 presents the energy spectra in the unburnt gases for both the lower- and the higher-Ka flames. First, it is important to note that, as expected, both profiles collapse on each other. Second, the presence of an inertial sub-range is very limited. This is to be expected given the turbulent Reynolds numbers. Finally, for both cases, the

turbulent kinetic energy is contained over two decades of length scales. This is also to be expected given the turbulent Reynolds numbers of approximately 100. This range of length scale is limited by the inherent computational cost.
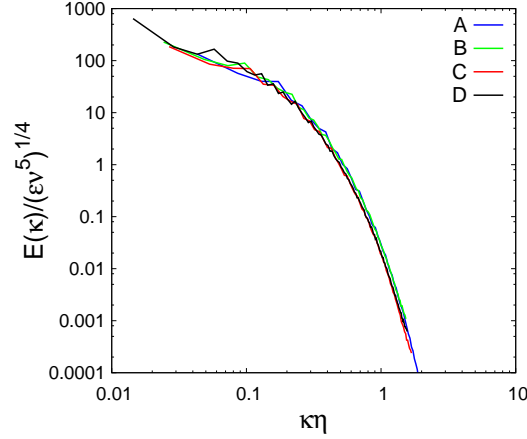

Fig. 5. Normalized two-dimensional three components spectra taken in a y-z plane in the unburnt gases (averaged over time). $\kappa = 2k\pi/L$, for $k = 1, 2, ..., N_y/2$, with N_y the number of points in the y- or z-direction, is the wavenumber.

4.3. Forcing analysis

As discussed previously, the implemented method of turbulence forcing intends to maintain a constant TKE throughout domain. Figure 6a displays the planar averaged TKE for case B, which, as expected, is nearly constant in the region of forcing. Next we consider the planar averaged dissipation rate, defined as $\bar{\epsilon} = \overline{\tau' : S''}/\bar{\rho}$ [43]. Figure 6b shows that this quantity is also constant in the region of forcing. This may be explained through the TKE transport equation for the case of statistical stationarity and homogeneity in the y and z directions,

$$\tilde{u}\frac{\partial k}{\partial x} = -\bar{\epsilon} + 2Ak_o - \widetilde{u''u''}\frac{\partial \tilde{u}}{\partial x} \tag{25}$$

$$+ \frac{1}{\bar{\rho}}\frac{\partial}{\partial x}\left(\overline{\boldsymbol{e}_x \cdot \tau \cdot \boldsymbol{u}''} + \frac{1}{2}\overline{u''\rho(\boldsymbol{u}'' \cdot \boldsymbol{u}'')} - \overline{P'u''}\right) - \frac{1}{\bar{\rho}}\overline{\tau} : \overline{S''} - \frac{\overline{u''}}{\bar{\rho}}\frac{\partial \overline{P}}{\partial x} + \frac{1}{\bar{\rho}}\overline{P'\nabla \cdot u''} \tag{26}$$

where $\boldsymbol{e}_x$ is the unit vector in the x direction. The first four terms in this equation, namely the left hand side (LHS), dissipation, forcing, and dilatation, respectively, are plotted in Fig. 6c along with with the residual, which represents the cumulative magnitude of all the remaining terms. Dissipation and forcing are the dominant terms, even through the flame.

Previous studies in 3D periodic homogeneous, isotropic turbulence found that linear forcing results in an integral length scale, $l = (2k/3)^{3/2}/\bar{\epsilon}$, which is proportional to the domain size [44], namely about $0.19L$. The integral length scale for the present configuration is fairly constant through the domain and acquires a value of approximately $0.16L$ (Fig. 6d).

4.4. Case B - Results overview

At high Karlovitz numbers, the spatial structure of a premixed flame is expected to depart from that of a laminar flame, as turbulent structures are sufficiently small enough to penetrate the preheat zone, and potentially the reaction zone. Figure 7 presents contours of vorticity, n-C_7H_{16} and CH_2O mass fractions, and temperature through the flame brush on a two-dimensional horizontal slice of the non-unity Lewis number turbulent flame. This figure is representative of both the unity and the non-unity Lewis number turbulent flame brushes.

As expected the preheat zone appears largely thickened [1] (approximately 10 times larger than the laminar flame). It is interesting to note that smaller turbulent structures are observed upstream of the flame (i.e. in the preheat zone) compared to close to the reaction zone. This is partially-explained by the fact that the kinematic viscosity increases (by up to a factor of 30) and the Kolmogorov length scale, $\eta = \left(\nu^3/\epsilon\right)^{1/4}$, increases through the flame by about a factor of 13.

8

(a) Turbulent kinetic energy.

(b) Dissipation rate.
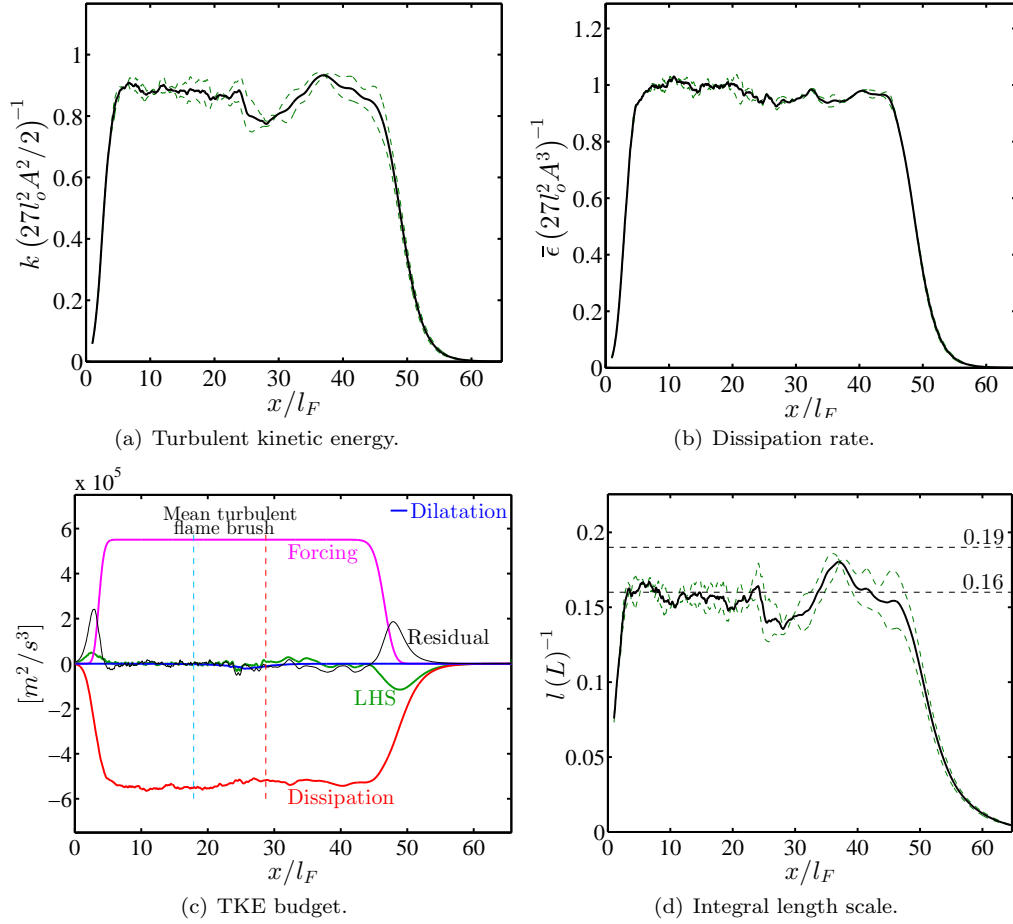
(c) TKE budget.

(d) Integral length scale.

Fig. 6. Planar and temporal average of turbulent kinetic energy, dissipation rate, and terms in the TKE transport equation, and integral length scale for case B. Green dashed lines correspond to averages when either the first or second half of the data is used; they are indicative of the statistical uncertainty in the computed averages.

5. Effective Lewis numbers

5.1. *Turbulent flame structure in the absence of differential diffusion*

To properly assess the influence of turbulence on the flame structure, one can analyze the correlation between species and temperature (or any other progress variable). As such, the flame structure can be adequately compared to that of a one-dimensional laminar flame, which is well represented in temperature space. Any departure from a one-dimensional laminar flame due to turbulence should be captured by these species mass fraction profiles.

In this sense, several species mass fractions are plotted against temperature and are compared to their one-dimensional laminar flame equivalent. Figure 8 shows joint probability densities of n-C_7H_{16}, C_2H_4, and CO_2 mass fraction, *vs.* temperature. These species correspond to a reactant, an intermediate species, and a product, respectively. The conditional mean of these species mass fraction (conditional on temperature) is also shown. This figure is representative of the overall flame structure as the mass fractions of other species show similar behaviors. These results suggest that the influence of turbulence on the flame structure in the absence of differential diffusion is very limited as the spread of the joint PDF is limited (this has also been observed by Aspden *et al.* for a high-Ka CH_4/air flame [6]). More interestingly, the conditional mean profiles of these species follow very closely the profiles of a one-dimensional, unstretched laminar flame at the same condition. This result is surprising, as the turbulent flame is clearly not in the flamelet regime and does not look like a flamelet.

In summary, while the turbulent flame is thickened by turbulence and is clearly not a thin flame, its *structure* is similar to that of a flamelet. This may suggest that the use of a progress variable with tabulated chemistry [45–47] would be justified and sufficient even at such high Karlovitz number.
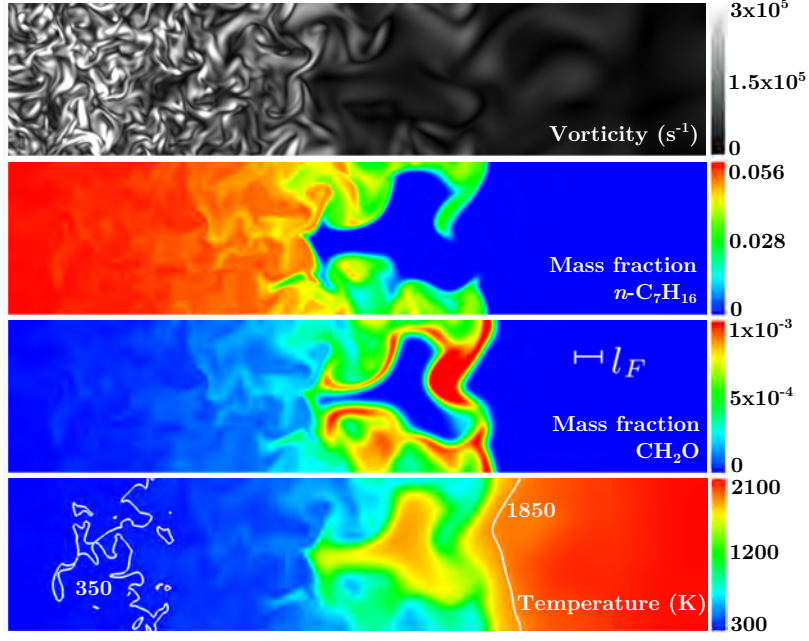
9

Fig. 7. Contours of vorticity, n-C_7H_{16} and CH_2O mass fractions, and temperature through the flame brush on a two-dimensional horizontal slice. The laminar flame thickness l_F is added for comparison.
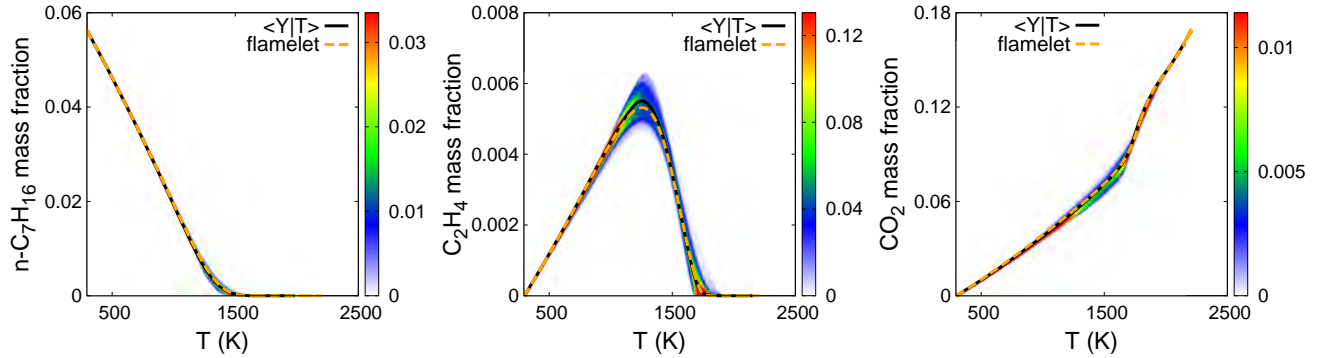

Fig. 8. Joint PDF and conditional mean (solid line) of the n-C_7H_{16} (top left), C_2H_4 (top right), and CO_2 (bottom) mass fraction *vs.* temperature from the unity Lewis number DNS. The unity Lewis number flamelet solution is also shown (dashed line).

5.2. *Turbulent flame structure with differential diffusion*

Similarly to Fig. 8, Fig. 9 presents the structure of C_2H_4 through the non-unity Lewis number flame. The full-transport flamelet solution is also added for comparison. While turbulence has almost no impact on the structure of the unity Lewis number flame, it has a clear effect on that of a non-unity Lewis numbers flame. In this case, the turbulent flame structure lies between that of a full transport and a unity Lewis number flamelet. Once again, a first order effect of turbulence on scalar transport is an increase in the effective diffusivity of each scalar (including species mass fractions and temperature) through increased mixing. As a result, the effective species Lewis number take the following from:

$$Le_{i,\text{eff}} = \frac{\alpha + D_T}{D_i + D_T}. \tag{27}$$

A similar expression for these effective Lewis numbers was first suggested by Peters [1]. Equation 27 suggests that if the turbulence were sufficiently intense, the non-unity Lewis number case would behave the same as the unity Lewis number case, *i.e.* turbulence would suppress differential diffusion effects.

5.2.1. *Effective Lewis numbers*

Any model should at least capture the mean of the turbulent flame (in a statistical sense). Reynolds-averaged transport equations provide information about the ensemble/statistical average of the transported quantity:
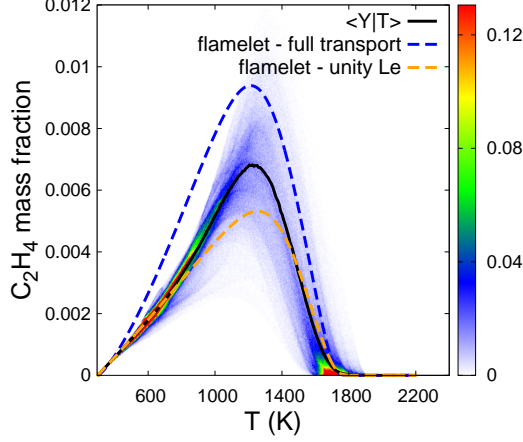
Fig. 9. Joint PDF and conditional mean (solid line) of the C_2H_4 mass fraction *vs.* temperature from the non-unity Lewis number DNS. The non-unity and unity Lewis number flamelet solutions are also shown (dashed line).

$$\frac{\partial}{\partial t}\left(\overline{\rho}\widetilde{Y}_i\right) + \nabla \cdot \left(\overline{\rho}\widetilde{\boldsymbol{u}}\widetilde{Y}_i\right) = \nabla \cdot \left[\overline{\rho}\left(D_i + D_T\right)\nabla\widetilde{Y}_i\right] + \overline{\dot{\omega}_i} \tag{28}$$

$$\frac{\partial}{\partial t}\left(\overline{\rho}\widetilde{T}\right) + \nabla \cdot \left(\overline{\rho}\widetilde{\boldsymbol{u}}\widetilde{T}\right) = \nabla \cdot \left[\overline{\rho}\left(\alpha + D_T\right)\nabla\widetilde{T}\right] + \overline{\left(\frac{\dot{\omega}_T}{c_p}\right)}, \tag{29}$$

where $\overline{\cdot}$ denotes a Reynolds average and $\widetilde{\cdot}$ a Favre average. D_T is the eddy diffusivity and is assumed to be identical for all species and temperature. This result is a direct consequence of assuming turbulence mixes all scalars the same way. A similar assumption is made in transported PDF methods [48,49]. From Eq. 28 and 29, an effective Lewis number can be obtained for each species:

$$Le_{i,\text{eff}} = \frac{D_{\text{heat}}}{D_{\text{mass}}} = \frac{\alpha + D_T}{D_i + D_T} = \frac{1 + \frac{D_T}{\alpha}}{\frac{1}{Le_i} + \frac{D_T}{\alpha}}. \tag{30}$$

Assuming that the eddy diffusivity scales as the product of the integral length scale and the velocity fluctuation, $D_T \propto lu'$, the model for the effective Lewis numbers can be expressed as

$$Le_{i,\text{eff}}^{\text{RANS}} = \frac{1 + a^{\text{RANS}} Re_T}{\frac{1}{Le_i} + a^{\text{RANS}} Re_T}, \tag{31}$$

where a proportionality constant a^{RANS} is used. With this approach, the effective Lewis number does not depend on any flame characteristic. This result is rather surprising as such a dependency should be expected.

Assuming that the eddy diffusivity is controlled by eddies of the size of the flame, $D_T \propto l_F u_F$, a model for the effective Lewis numbers follows

$$Le_{i,\text{eff}}^{l_F} = \frac{1 + a^{l_F} Ka^{2/3}}{\frac{1}{Le_i} + a^{l_F} Ka^{2/3}}, \tag{32}$$

where a^{l_F} is a proportionality constant.

A third approach is to consider the response time of the flame to unsteady perturbations. This response time is expected to scale like the flame time t_F, *i.e.* $D_T \propto l(t_F)u(t_F)$. The model for the effective Lewis numbers becomes

$$Le_{i,\text{eff}}^{t_F} = \frac{1 + a^{t_F} Ka^2}{\frac{1}{Le_i} + a^{t_F} Ka^2}, \tag{33}$$

where a proportionality constant a^{t_F} is used.

Finally, it was found that an additional empirical model in which the Re_T is simply replaced by Ka performs better for a series of hydrogen/air turbulent premixed flames. This model is given by

$$Le_{i,\text{eff}}^{Ka} = \frac{1 + a^{Ka} Ka}{\frac{1}{Le_i} + a^{Ka} Ka}. \tag{34}$$

5.3. Comparison with DNS data

The Ka-based model (Eq. 34) is used to compute a set of effective species Lewis numbers. The solution of an unstretched laminar flame with this set of effective species Lewis numbers is obtained with FlameMaster. The species
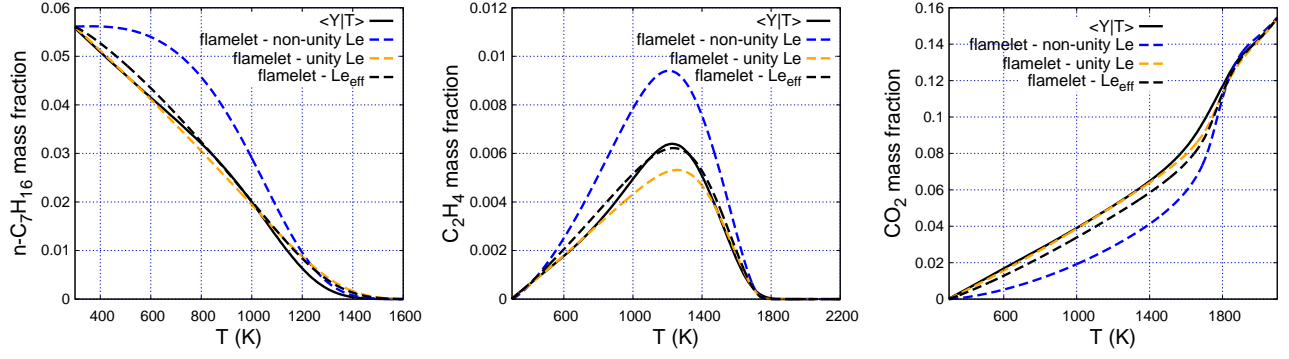
Fig. 10. Conditional mean (solid line) of the $n\text{-}C_7H_{16}$ (top left), C_2H_4 (top right), and CO_2 (bottom) mass fraction *vs.* temperature. The non-unity, the unity, and the effective Lewis number flamelet solutions are also shown (dashed line).

mass fraction *vs.* temperature profiles are compared, in Fig. 10, to the corresponding conditional means from the DNS for the fuel, C_2H_4, and CO_2. Although differences are noticeable, especially for the product, the effective Lewis number model captures fairly well the effect of turbulent mixing on the mean flame structure.

6. Reaction zone

6.1. *Overview*

Contours of the source term of $n\text{-}C_7H_{16}$ and H_2O for the non-unity Lewis number B flame are shown in Fig. 11 on the same two-dimensional slice as in Fig. 7. For a Karlovitz numbers as large as 220, scaling arguments suggest that turbulent structures should be sufficiently small enough to penetrate the reaction zone [1]. However, two observations can be made from Fig. 11: 1) the reaction zone appears to be thin and 2) signs of local extinctions (broken reaction zone) can be observed in the fuel consumption zone, but cannot be observed in the H_2O production zone.

The first observation could seem inconsistent with the fact that the Kolmogorov length scale in the unburnt gas is 10 times smaller than the laminar reaction zone thickness. However, as mentioned above, the Kolmogorov length scale increases through the flame due to the increasing kinematic viscosity, and becomes as large as the laminar reaction zone thickness as it reaches the burnt side.
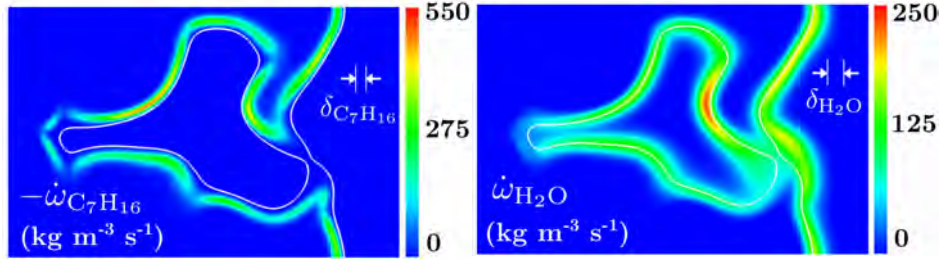

Fig. 11. Contours of the source terms of $n\text{-}C_7H_{16}$ (left) and H_2O (right) on the same two-dimensional horizontal slice as in Fig. 7. The isoterm $T = 1500$ K (white) is also shown. The laminar reaction zone thicknesses (full width at half-height) of $n\text{-}C_7H_{16}$ ($\delta_{C_7H_{16}}$) and H_2O (δ_{H_2O}) are also shown for comparison.

6.2. *Fuel consumption at T_{peak}*

To investigate the impact of turbulence on the reaction zone, Fig. 12(a) shows the joint probability density of the normalized fuel consumption rate as a function of temperature for the unity Lewis number flame. The mean of the source term conditional to temperature is also shown. This profile is compared to its unstretched one-dimensional flame equivalent. While the mean profile is very close to that of the one-dimensional flame, fluctuations around this mean are relatively large. Alternatively, Fig. 12(b) presents the joint probability density of the fuel consumption term away from the flame front (at local temperature T) normalized by the consumption term of the closest point on the flame front (*i.e.* normaly projected on the iso-surface $T = T_{\text{peak}}$). As can be observed, the fluctuations are significantly reduced now. Figure 12(c) shows the same normalized source term for the non-unity Lewis number case. These plots suggest that fuel consumption locally scales like its value at T_{peak}, for both the unity and the non-unity Lewis number flames, *i.e.*
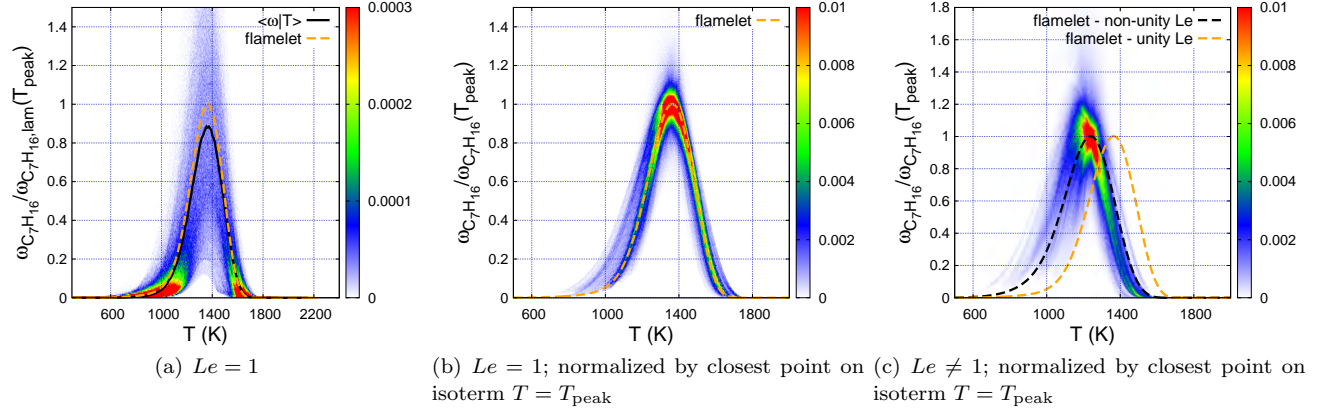
(a) $Le = 1$

(b) $Le = 1$; normalized by closest point on isoterm $T = T_{\mathrm{peak}}$

(c) $Le \neq 1$; normalized by closest point on isoterm $T = T_{\mathrm{peak}}$

Fig. 12. (a)Joint PDF and conditional mean (solid line) of n-$\mathrm{C_7H_{16}}$ source term, $\dot{\omega}_{\mathrm{C_7H_{16}}}$, normalized by its peak laminar value $vs.$ temperature from the unity Lewis number simulation. Joint PDF of n-$\mathrm{C_7H_{16}}$ source term, $\dot{\omega}_{\mathrm{C_7H_{16}}}$, normalized, in the direction normal to the isoterm $T = T_{\mathrm{peak}}$, by its value on this isoterm $vs.$ temperature for the unity Lewis number (b) and the non-unity Lewis number DNS (c). The non-unity and unity Lewis number flamelet solutions are also shown (dashed line).

$$\dot{\omega}_{\mathrm{C_7H_{16}}}(T) \approx \dot{\omega}_{\mathrm{C_7H_{16}}}(T_{\mathrm{peak}}) \frac{\dot{\omega}_{\mathrm{C_7H_{16},lam}}(T)}{\dot{\omega}_{\mathrm{C_7H_{16},lam}}(T_{\mathrm{peak}})}. \tag{35}$$

Therefore, only the fuel conssumption term at $T = T_{\mathrm{peak}}$ will be further considered.

6.3. *Curvature and strain rate*

The mean curvature is expressed as

$$\kappa = \nabla \cdot \boldsymbol{n}, \tag{36}$$

where $\boldsymbol{n} = -\nabla T / |\nabla T|$ is the normal to the reaction zone surface, and is positively oriented towards the unburnt gas. The probability density distribution of curvature is presented in Fig. 13(a) for both the unity and the non-unity Lewis number cases. First, it is important to note that the magnitude of curvature is very large, and such intense curvatures are difficult to observe in laminar flames. Second and most importantly, no differential diffusion effect is visible in Fig. 13(a), suggesting that the geometry of the reaction surface is only influenced by turbulence.
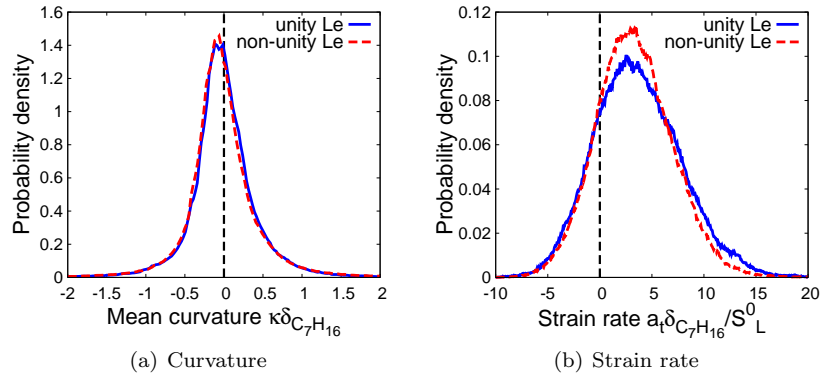

(a) Curvature

(b) Strain rate

Fig. 13. Probability density function, on the reaction surface, of κ, normalized by the laminar reaction zone thickness (top), and a_t, normalized by the ratio of the laminar reaction zone thickness to the laminar flame speed (bottom).

The strain rate tangential to the reaction surface is computed as, similarly to Refs. [50,51],

$$a_t = \nabla \cdot \boldsymbol{u} - \boldsymbol{n} \cdot \nabla \boldsymbol{u} \cdot \boldsymbol{n}, \tag{37}$$

where $\boldsymbol{u}$ is the velocity. Figure 13(b) shows the probability density of the normalized strain rate tangential to the reaction surface. The magnitude of the strain rate, up to 70,000 $\mathrm{s^{-1}}$, is very large and hard to reproduce in laminar flames. Again, the strain rate applied to both the unity Lewis number and the non-unity Lewis number reaction surface are similar. Consistent with values previously-reported by several authors for methane/air and hydrogen/air flames in the thin reaction zone [51–54], a positive mean tangential strain rate is observed.

With the information presented in this section, it is interesting to consider the following expression (often used to predict the effects of strainrate and curvature)

13

$$\frac{S_L}{S_L^0} = 1 - \frac{\mathcal{L}}{\delta_{\mathrm{C_7H_{16}}}} \left(\kappa \delta_{\mathrm{C_7H_{16}}} + \frac{a_t \delta_{\mathrm{C_7H_{16}}}}{S_L^0} \right). \tag{38}$$

Under similar unburnt conditions (but with an unburnt temperature of 353K), $\mathcal{L} \approx 1\mathrm{mm}$ [55], which means $\mathcal{L}/\delta_{\mathrm{C_7H_{16}}} \sim \mathcal{O}(10)$. Figure 13 shows that $\kappa \delta_{\mathrm{C_7H_{16}}} \sim \mathcal{O}(0.1)$–$\mathcal{O}(1)$,and $a_t \delta_{\mathrm{C_7H_{16}}}/S_L \sim \mathcal{O}(1)$–$\mathcal{O}(10)$, which means that $\mathcal{L}(\kappa + a_t/S_L) \gg 1$ and Eq. 38 does not hold anymore.

6.4. *Propagating vs. material surface*

The previous results suggest that differential diffusion virtually does *not* affect the reaction zone geometry. This is a consequence of the high Karlovitz number and can be explained by an analogy to the work of Yeung *et al.* [56] who analyzed theoretically and numerically the geometry of material and propagating surfaces in the presence of homogeneous isotropic turbulence. Yeung *et al.* [56] found that a material surface orientates preferentially with the strain rate tensor. They identified a universal distribution of strain rate on the material surface. In particular, they observed that 80% of the strain rate is positive. They further argued that a propagating surface (with speed w) has the same strain rate distribution as a material surface, independently of the turbulent Reynolds number, under the condition $w/v_\eta \ll 1$, where v_η is the Kolmogorov velocity.

For the present flames analyzed, 81% and 82% of the strain rate was found to be positive for the unity and the non-unity Lewis number flames, respectively. These results are consistent with the ratios S_L^0/v_η as listed in Table 3. These results are also consistent with the series of DNS of lean $\mathrm{H_2}$/air turbulent flames conducted by Aspden *et al.* [5].

Fuel	Ka	S_L^0/v_η	% $a_t > 0$
n-$\mathrm{C_7H_{16}}$/air ($Le = 1$)	280	0.08	81
n-$\mathrm{C_7H_{16}}$/air ($Le \neq 1$)	220	0.11	82
$\mathrm{H_2}$/air	28	0.30	80
$\mathrm{H_2}$/air	4200	0.02	80

Table 3
S_L^0/v_η ratios (see Ref. [56]) and curvature and strain rate statistics for the flames presented in this thesis and for two lean $\mathrm{H_2}$/air ($\phi = 0.4$) flames presented in [5]. v_η is evaluated at T_{peak}.

The overall conclusion is that the reaction zone surface behaves as a material surface under the intense turbulent field. Even if the local consumption rates are affected, they are too weak to alter the shape of the flame front. As such, the distributions of curvature and strain rate are independent from differential diffusion effects.

6.5. *Turbulent flame speed*

The turbulent flame speed may be expressed as

$$S_T = \frac{1}{\rho_u Y_{\mathrm{C_7H_{16}},u} L^2 (t_2 - t_1)} \int_{t_1}^{t_2} \int_{\Omega} -\dot{\omega}_{\mathrm{C_7H_{16}}}(x,y,z,t) \, \mathrm{d}V \mathrm{d}t, \tag{39}$$

where the subscript u is used for unburnt conditions, $t_2 - t_1$ is the data collection time. The values obtained are presented in Table 4.

The difference in the S_T/S_L ratios (between unity and non-unity Lewis numbers) highlights an important differential diffusion effect (the only difference between the flames). The unity Lewis number flame encounters a significantly larger increase in flame speed than the non-unity Lewis number flame, although both flames are subjected to the same incoming turbulent flow. As observed by many authors [57–64], this further suggests that differential diffusion has to be taken into account in turbulent flame speed models (*e.g.* in the form of a Lewis number dependence).

Although the latter observation is interesting in itself, a better understanding of where this difference comes from is necessary for modeling purposes. Even if the current flames are not in the (thin) corrugated flamelet regime, the reaction zone remains thin and is only weakly corrugated. As a consequence, a reaction surface (isocontour $T = T_{\mathrm{peak}}$) and a local consumption speed can still be defined. For the present analysis, a similar approach to that used by Damköhler for the corrugated flamelet regime is taken [65].

As shown in Fig. 12(b) and 12(c), the profiles of $\dot{\omega}_{\mathrm{C_7H_{16}}}$ in the direction normal to the reaction surface remain fairly unchanged when scaled by their value at $T = T_{\mathrm{peak}}$. Hence, using Eq. 35 in Eq. 39, the turbulent flame speed can be approximated as

$$S_T \approx S_L^0 \frac{A_T}{A} \left\langle \frac{\dot{\omega}_{\mathrm{C_7H_{16}}}}{\dot{\omega}_{\mathrm{C_7H_{16}},\mathrm{lam}}} \right\rangle_{T_{\mathrm{peak}}}, \tag{40}$$

where $\langle \dot{\omega}_{\mathrm{C_7H_{16}}}/\dot{\omega}_{\mathrm{C_7H_{16}},\mathrm{lam}} \rangle_{T_{\mathrm{peak}}}$ is surface-weighted and averaged in time. A_T is defined as the surface area of the reaction zone surface as shown in Fig. 14. These values are presented in Table 4 for the present flames. Once again,
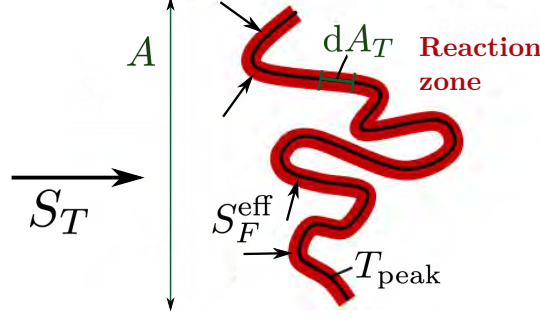
14

Fig. 14. Schematic drawing to illustrate Eq. 40. $S_F^{\text{eff}} = \left\langle \dot{\omega}_{\text{C}_7\text{H}_{16}}/\dot{\omega}_{\text{C}_7\text{H}_{16},\text{lam}} \right\rangle_{T_{\text{peak}}} \cdot S_L^0$ is used.

differential diffusion has a limited effect on the turbulent surface area: the flame acts as a material surface. Second, the values presented are in very good agreement with Eq. 40. Third, the main contribution to the differences in turbulent flame speed due to differential diffusion appears in the $\left\langle \dot{\omega}_{\text{C}_7\text{H}_{16}}/\dot{\omega}_{\text{C}_7\text{H}_{16},\text{lam}} \right\rangle_{T_{\text{peak}}}$ ratio.

	unity Le_i	non-unity Le_i
S_T (m/s)	1.06	0.69
S_T/S_L^0	3.7	1.9
A_T/A	3.5 ± 1.0	2.9 ± 0.8
$\left\langle \dfrac{\dot{\omega}_{\text{C}_7\text{H}_{16}}}{\dot{\omega}_{\text{C}_7\text{H}_{16},\text{lam}}} \right\rangle_{T_{\text{peak}}}$	1.00	0.66
$\dfrac{A_T}{A} \left\langle \dfrac{\dot{\omega}_{\text{C}_7\text{H}_{16}}}{\dot{\omega}_{\text{C}_7\text{H}_{16},\text{lam}}} \right\rangle_{T_{\text{peak}}}$	3.5	1.9
$A_{5\%}/A_T$	0%	2.9%
$A_{100\%}/A_T$	56.4%	76.6%

Table 4
Ratios relevant to the turbulent flame speed (see Eq. 40). Confidence intervals correspond to plus or minus one standard deviation.

For the unity Lewis number case, only strain rate has an effect on the fuel consumption rate (see Fig. 15(a)). This effect is approximately symmetric with respect to the mean strain rate and this strain rate is symmetrically distributed with respect to its mean (see Fig. 13(b)). Therefore, a close-to-unity $\langle \dot{\omega}_{\text{C}_7\text{H}_{16}}/\dot{\omega}_{\text{C}_7\text{H}_{16},\text{lam}} \rangle_{T_{\text{peak}}}$ ratio is expected. This is consistent with results previously reported for turbulent flames with a close-to-unity fuel Lewis number [50,52,66].

For the non-unity Lewis number case, the fuel consumption rate is correlated with curvature (see Fig. 15(b)). While curvature is symmetrically distributed with respect to its mean, its effect on the fuel consumption term is highly non-linear and is not symmetric with respect to its mean. Consequently, the overall effect is a reduction in the average fuel consumption rate, *i.e.* $\langle \dot{\omega}_{\text{C}_7\text{H}_{16}}/\dot{\omega}_{\text{C}_7\text{H}_{16},\text{lam}} \rangle_{T_{\text{peak}}} < 1$.
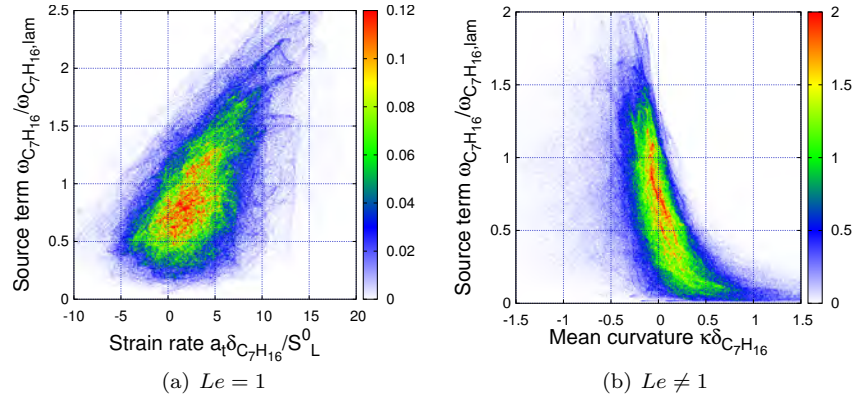

(a) $Le = 1$

(b) $Le \neq 1$

Fig. 15. Joint probability density function, on the isoterm $T = T_{\text{peak}}$, of n-C_7H_{16} source term, $\dot{\omega}_{\text{C}_7\text{H}_{16}}$, normalized by its peak laminar value *vs.* the normalized tangential strain rate for $Le = 1$ and by the normalized mean curvature for $Le \neq 1$.

15

6.6. *Summary*

The flow chart presented in Fig. 16 illustrates the mechanism through which turbulence and differential diffusion affect the overall turbulent flame speed and summarizes the main results of this section.
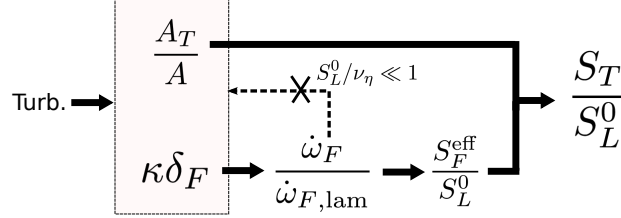

Fig. 16. Flow chart illustrating the mechanism through which turbulence affects the flame speed for the flames presented in this work.

7. Modeling the reaction zone

For flames A and B, the following results were identified:
(i) largely thickened preheat zone, yet thin reaction zone (see Fig. 11),
(ii) large burning rate fluctuations around the mean profile *vs.* progress variable,
(iii) for unity Lewis numbers:

$$< \dot{\omega}_F | c > \approx \dot{\omega}_{F,\text{lam}} (c) , \tag{41}$$

(iv) for non-unity Lewis numbers:

$$< \dot{\omega}_F | c > \neq \dot{\omega}_{F,\text{lam}} (c) , \tag{42}$$

(v) for both cases:

$$\dot{\omega}_F (\mathbf{x}, t) \neq \dot{\omega}_F (c (\mathbf{x}, t)) . \tag{43}$$

This section is directly related to point 5, *i.e.* the objective is to identify a set of variables $\boldsymbol{\psi}$ such that $\dot{\omega}_F (\mathbf{x}, t)$ can be approximated accurately by $\dot{\omega}_F (c (\mathbf{x}, t), \boldsymbol{\psi} (\mathbf{x}, t))$, while keeping the dimensionality of $\boldsymbol{\psi}$ small.

7.1. *Coordinate transformation*

In order to identify the set of variables $\boldsymbol{\psi}$, a similar approach to the one used in Ref. [25] for non-premixed flames is taken in this section. The following coordinate transformation is proposed:

$$(x_1, x_2, x_3, t) \rightarrow (c (x_1, x_2, x_3, t), c_2 (x_1, x_2, x_3, t), c_3 (x_1, x_2, x_3, t), \tau) , \tag{44}$$

with

$$\nabla c \cdot \nabla c_2 = 0, \qquad \text{and} \qquad \nabla c \cdot \nabla c_3 = 0, \tag{45}$$

i.e. the variables c_2 and c_3 lie in the surface of constant c. The only assumption made in this section is that the Jacobian of the transformation is not singular. Applying the coordinate transformation to Eq. 5, the following transformed equations for the species mass fractions are obtained:

$$\underbrace{\left\{\nabla\cdot\left[\rho\alpha\left(\frac{1}{Le_c}-\frac{1}{Le_i}\right)\nabla c\right]+\nabla\cdot\left(\rho\sum_{j=1}^{N}b_jY_j\mathbf{V_{c,j}}\right)+\dot{\omega}_c\right\}\frac{\partial Y_i}{\partial c}}_{\text{normal convection}}\tag{46}$$

$$-\underbrace{\frac{\rho\chi}{2Le_i}\frac{\partial^2 Y_i}{\partial c^2}}_{\text{normal diffusion}}-\underbrace{\dot{\omega}_i}_{\text{chemical source}}-\underbrace{\nabla\cdot(\rho Y_i\mathbf{V_{c,i}})}_{\text{velocity correction}}$$

$$=-\rho\frac{\partial Y_i}{\partial\tau}-\underbrace{\rho\sum_{k=2}^{3}\left[\frac{\partial Y_i}{\partial c_k}\left(\frac{\partial c_k}{\partial t}+\mathbf{u}\cdot\nabla c_k\right)\right]}_{\text{Lagrangian transport}}$$

$$+\underbrace{\sum_{k=2}^{3}\frac{\rho\chi_k}{2Le_i}\frac{\partial^2 Y_i}{\partial c_k^2}+\frac{2\rho\alpha}{Le_i}\left(\nabla c_2\cdot\nabla c_3\right)\frac{\partial^2 Y_i}{\partial c_2\partial c_3}}_{\text{tangential diffusion}}$$

$$+\underbrace{\nabla\cdot\left(\frac{\rho\alpha}{Le_i}\nabla c_2\right)\frac{\partial Y_i}{\partial c_2}+\nabla\cdot\left(\frac{\rho\alpha}{Le_i}\nabla c_3\right)\frac{\partial Y_i}{\partial c_3}}_{\text{tangential convection}},$$

where $\chi=2\alpha|\nabla c|^2$ and $\chi_k=2\alpha|\nabla c_k|^2$ for $k=2,3$ are the dissipation rates of c, c_2, and c_3, respectively. In the above equations, the Lagrangian transport corresponds to the convection of the scalar, in the c_2-c_3-direction, *i.e.* in the surface of iso-c, induced by the Lagrangian transport of these c_2 and c_3 coordinates. The normal terms correspond to convection or diffusion of the scalar in the c-direction, whereas the tangential terms correspond to convection or diffusion of the scalar in the c_2-c_3-direction.

7.2. *Flamelet equations - Unity Lewis number*

Recall that, in the regime considered, the reaction zone is considered to be thin. It is therefore assumed that, in the vicinity of the reaction zone, $\partial/\partial c_k << \partial/\partial c$, for $k=2,3$. Furthermore, assuming the dependence in τ in the transformed coordinate system is negligible, the flamelet equations are obtained:

$$\underbrace{\dot{\omega}_c\frac{\mathrm{d}Y_i}{\mathrm{d}c}}_{\text{convection}}=\underbrace{\frac{\rho\chi}{2}\frac{\mathrm{d}^2Y_i}{\mathrm{d}c^2}}_{\text{diffusion}}+\underbrace{\dot{\omega}_i}_{\text{chemical source}}\tag{47}$$

These equations form a system of ordinary differential equations in which the Y_i are the unknowns, c is the variable, and the dissipation rate $\chi(c)$ is the parameter. Each of the terms in the above equations are only a function of c and χ.

Given the form of the flamelet equations, the fuel burning rate should solely be a function of the progress variable c and its dissipation rate χ. In contrast with Fig. 15(a) and 15(b) shown previously, Fig. 17 presents the joint probability density function of the fuel consumption rate *vs.* the dissipation rate of the progress variable. It is clear that the fuel burning rate is far more correlated with χ than with strain-rate. Physically, this means that turbulence affects the fuel burning rate by compressing or extending the isosurfaces of the progress variable. The figure also shows that the solution of the flamelet equations (Eq. 47) provide a very good estimate of the dependence of the chemical source term on the dissipation rate.

7.3. *Flamelet equations - Non-unity Lewis number*

Once again, we make the same assumptions of local one-dimensionality in phase space, *i.e.* $\partial/\partial c_k << \partial/\partial c$, for $k=2,3$, and steady state in phase space, *i.e.* $\partial/\partial\tau=0$, but no assumption is made on the species Lewis numbers. Let $\xi=\nabla\cdot(\rho\alpha\nabla c)$. Then, non-unity Lewis number flamelet equations become

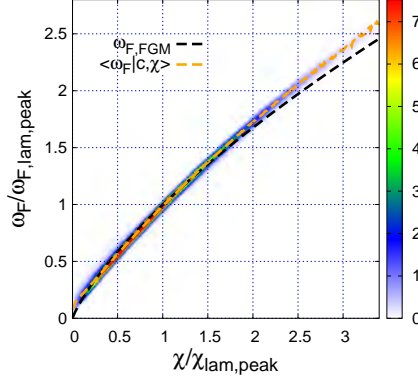Fig. 17. Comparison between the fuel burning rate predicted by $\dot{\omega}_{F,\mathrm{FGM}}(c,\chi)$ and $<\dot{\omega}_F|(c,\chi)>$ as a function of the dissipation rate, normalized by their peak laminar values, given $c = c_{\mathrm{peak}}$. The joint PDF on the isosurface of $c = c_{\mathrm{peak}}$ for the unity Lewis number flame B is also shown for comparison.

$$\underbrace{\dot{\omega}_c \frac{\mathrm{d}Y_i}{\mathrm{d}c}}_{\text{convection}} = \underbrace{\frac{\rho\chi}{2Le_i}\frac{\mathrm{d}^2 Y_i}{\mathrm{d}c^2}}_{\text{diffusion}} + \underbrace{\dot{\omega}_i}_{\text{chemical source}} \tag{48}$$

$$+ \underbrace{\left[\xi\left(\frac{1}{Le_i} - \frac{1}{Le_c}\right) + \frac{\rho\chi}{2}\frac{\mathrm{d}}{\mathrm{d}c}\left(\frac{1}{Le_i} - \frac{1}{Le_c}\right)\right]\frac{\mathrm{d}Y_i}{\mathrm{d}c}}_{\text{differential diffusion-induced convection}}$$

$$+ \underbrace{\nabla\cdot(\rho Y_i \mathbf{V_{c,i}}) - \sum_{j=1}^{N} b_j \nabla\cdot(\rho Y_j \mathbf{V_{c,j}})\frac{\mathrm{d}Y_i}{\mathrm{d}c}}_{\text{velocity correction}},$$

In this set of equations, a second parameter, $\xi(c)$, is involved. It corresponds to the diffusion of c in the original coordinate system. Note that, as one would expect, this parameter includes curvature effects.

Figure 18 shows the probability density function of the point-wise comparison in flame B between the predicted and the actual fuel burning rate, for three different optimal estimators: $<\dot{\omega}_F|c>$, $<\dot{\omega}_F|c,\chi>$, and $<\dot{\omega}_F|c,\chi,\xi>$. The inclusion of the third parameter leads to obvious improvements.

(a) $<\dot{\omega}_F|c>$ vs. $\dot{\omega}_F(\mathbf{x},t)$

(b) $<\dot{\omega}_F|c,\chi>$ vs. $\dot{\omega}_F(\mathbf{x},t)$

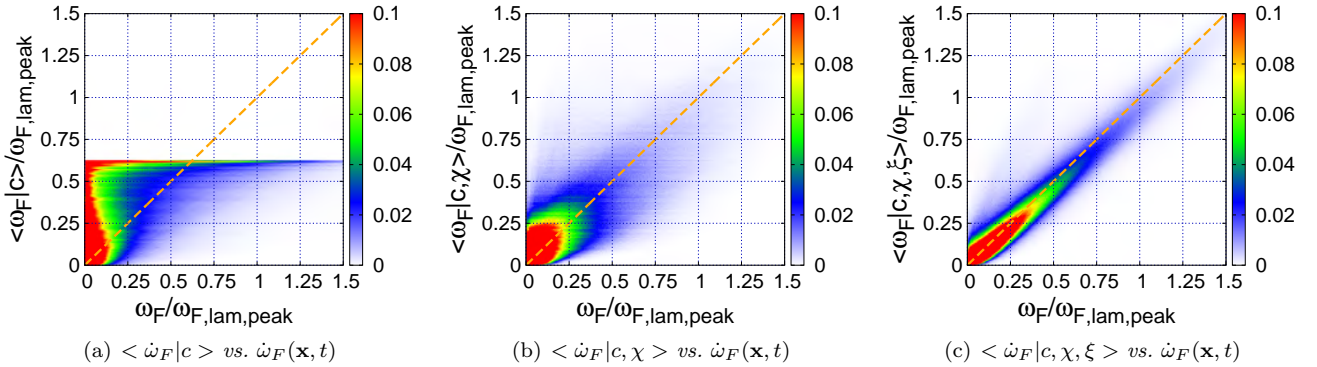(c) $<\dot{\omega}_F|c,\chi,\xi>$ vs. $\dot{\omega}_F(\mathbf{x},t)$

Fig. 18. Joint PDF of the comparison between the predicted fuel burning rate and the actual burning rate in the higher-Ka non-unity Lewis number flame.

7.4. Summary

While the flames considered in this work have a thin reaction zone, large fluctuations around the mean burning rate (conditional on c) were observed. In order to model these fluctuations, a coordinate transformation was performed, and the following results were identified:

(i) for the unity Lewis number flames,

    (a) the turbulent flames can be well represented by a set of one-dimensional (in c-space) flamelet equations parameterized by $\chi(c)$,

      (b) the fuel burning rate $\dot{\omega}_F(\mathbf{x}, t)$ can be approximated accurately by $\dot{\omega}_F(c(\mathbf{x}, t), \chi(\mathbf{x}, t))$,

      (c) the fuel burning rate is well predicted *a priori* by the solution to the set of flamelet equations,

  (ii) for the non-unity Lewis number flames,

      (a) the fuel burning rate $\dot{\omega}_F(\mathbf{x}, t)$ can be approximated accurately (only to some extent in the higher-Ka flame) by $\dot{\omega}_F(c(\mathbf{x}, t), \chi(\mathbf{x}, t), \xi(\mathbf{x}, t))$,

      (b) the fuel burning rate cannot be predicted *a priori* by the solution to the set of flamelet equations, unless a model for the effective diffusivities as a function of the progress variable is considered (future work),

      (c) the source term of the progress variable (relevant to a turbulent flame simulation with this reduced chemistry) can be closed by an *a posteriori* DNS-generated manifold.

Finally, it is important to note that the assumption of a thin reaction zone was made to obtain the premixed flamelet equations. While this assumption is valid in the thin reaction zone regime, it may not be the case for higher turbulence intensities corresponding to the distributed burning regime.

8. Overview of turbulent flow

8.1. *Conditional averaging*

Turbulence quantities are expected to vary through the flame based upon the local thermodynamic properties of the fluid (such as density and viscosity). In a curved and instantaneously transient flame, these quantities correlate better with a flame progress variable, denoted as C, compared to the spatial coordinate x. For this reason, averages are conditioned on C and denoted as

$$\langle \psi | C \rangle \tag{49}$$

The form of the progress variable chosen is $C = Y_{H_2O} + Y_{H_2} + Y_{CO_2} + Y_{CO}$, as it tracks the flame evolution through the preheat and reaction zones. The progress variable range is standardized by considering $\hat{C} = C/C_{max}$ so that 0 represents the reactants and 1 represents the products. By use of this conditional averaging, we define the local Kolmogorov time, length, and velocity scales as

$$\tau_\eta(C) = \left(\frac{\langle \nu | C \rangle}{\langle \epsilon | C \rangle} \right)^{1/2}, \tag{50}$$

$$\eta(C) = \left(\frac{\langle \nu | C \rangle^3}{\langle \epsilon | C \rangle} \right)^{1/4}, \tag{51}$$

$$u_\eta(C) = (\langle \epsilon | C \rangle \langle \nu | C \rangle)^{1/4}, \tag{52}$$

the local Karlovitz number as $Ka(C) = \tau_F/\tau_\eta(C)$, and the dissipation rate conditioned on C as $\langle \epsilon | C \rangle = \langle \tau' : S'' | C \rangle / \langle \rho | C \rangle$. Additionally, we define a quantity involving the flame density change, $\gamma(C) = \Delta\rho/\langle \rho | C \rangle$, where $\Delta\rho = \rho_u - \rho_b$, which will be used in the subsequent analysis.

8.2. *Vorticity overview*

First, the transformation of vorticity is qualitatively observed by plotting the vorticity magnitude through the flame. Figure 19 displays instantaneous 2D contours of cases A, B, C, D and E. The change in vorticity is dramatic as the magnitude is greatly suppressed through the flame. Preliminary observation suggests the vorticity is reduced to a lesser extent in cases C and D, which have a similar Ka_u as B and E, respectively, but a higher unburnt temperature.

9. Enstrophy budget

The enstrophy, $\omega^2 = \boldsymbol{\omega} \cdot \boldsymbol{\omega}$, transport equation is derived from the momentum equation as

$$\frac{1}{2} \frac{D\omega^2}{Dt} = \boldsymbol{\omega} \cdot S \cdot \boldsymbol{\omega} - \omega^2 (\nabla \cdot \boldsymbol{u}) + \frac{\boldsymbol{\omega}}{\rho^2} \cdot (\nabla\rho \times \nabla P) + \boldsymbol{\omega} \cdot \nabla \times \left(\frac{1}{\rho} \nabla \cdot \tau \right) + \boldsymbol{\omega} \cdot \nabla \times \frac{\boldsymbol{f}}{\rho},$$

where D/Dt is the material or total derivative. Each term on the right hand side is associated with a specific physical processes: vortex stretching, dilatation, baroclinic torque, viscous dissipation, and forcing, respectively. Vortex stretching, viscous dissipation, and forcing are active in constant density flows, while dilatation and baroclinic torque arise here only due to the presence of the flame. The change of fluid properties (such as density and viscosity) within a premixed flame alters the enstrophy of the incoming turbulence through these five terms.

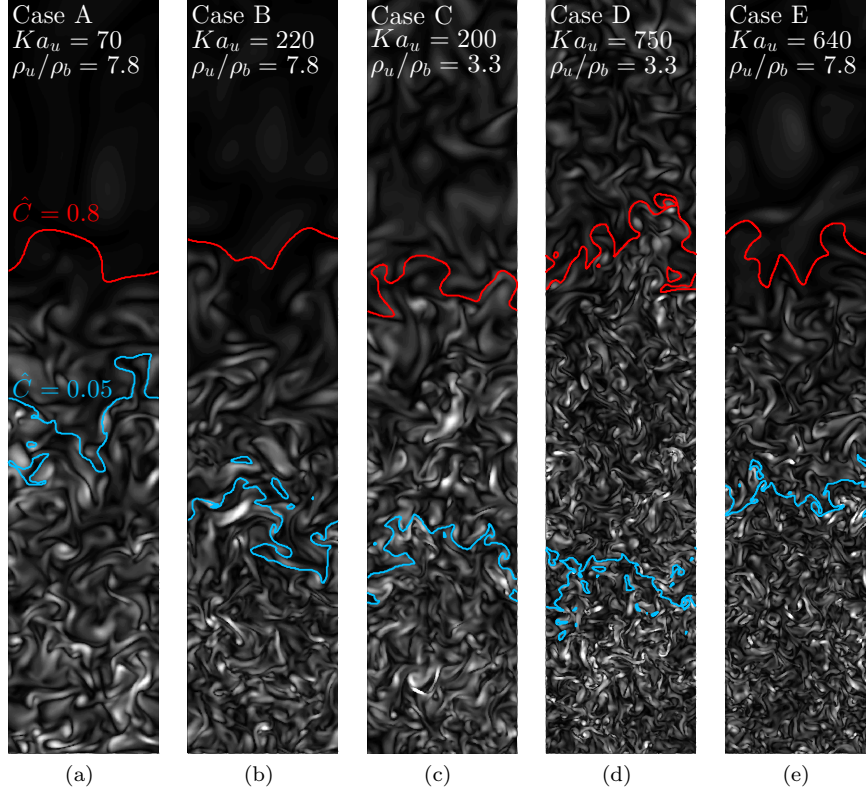In the following, a scaling for each term is provided. Only the first term is detailed.

Fig. 19. Two-dimensional slices of vorticity magnitude for cases A, B, C, D and E. Each figure corresponds to a region of size $L \times 5L$ and the flow direction is from bottom to top. The contours range between $[0; 2.1e5\ s^{-1}]$, $[0; 6.2e5\ s^{-1}]$, $[0; 5.5e6\ s^{-1}]$, $[0; 2.1e7\ s^{-1}]$, and $[0; 1.7e6\ s^{-1}]$, respectively. Blue and red contours represent the extent of the turbulent flame brush defined as the iso-surfaces of $\hat{C} = 0.05$ and $\hat{C} = 0.8$.

9.1. *Vortex stretching*

In dimensional form, the vortex stretching term can vary by more than an order of magnitude across the flame and varies by several orders of magnitude between the different cases (Fig. 20a). Scaling of this term requires estimates for vorticity and the rate of strain tensor.

In the present configuration of high Karlovitz number ($Ka_u > 70$), we estimate the magnitude of S with $1/\tau_\eta$. This result is consistent with homogeneous, isotropic turbulence where $\overline{S' : S'}$ also scales as $(1/\tau_\eta^2)$ [67]. As a spatial gradient of velocity, like the rate of strain tensor, vorticity is estimated as $1/\tau_\eta$ and enstrophy with $1/\tau_\eta^2$. Previous experimental and numerical work supports a correlation of vorticity with the Kolmogorov time scale under conditions of homogeneous, isotropic turbulence [68–70]. The above analysis results in the scaling,

$$\boldsymbol{\omega} \cdot S \cdot \boldsymbol{\omega} \propto \frac{1}{\tau_\eta^3}. \tag{53}$$

Normalized according to the above expression, the vortex stretching terms for each case collapse to a fairly constant value close to 0.15, which is the same value obtained in DNS of homogeneous, isotropic turbulence (Fig. 20b). The success of the normalization suggests that within the flame the vortex stretching term behaves similar to homogeneous, isotropic turbulence in the limit of high Karlovitz number.

9.2. *Dilatation*

Dilatation in the present configuration is due only to the effects of the flame. Scaling the dilatation term requires estimates of enstrophy and the divergence of velocity. This leads to the following scaling,

$$\omega^2(\nabla \cdot \boldsymbol{u}) \propto \gamma \frac{S_L}{l_F \tau_\eta^2}. \tag{54}$$
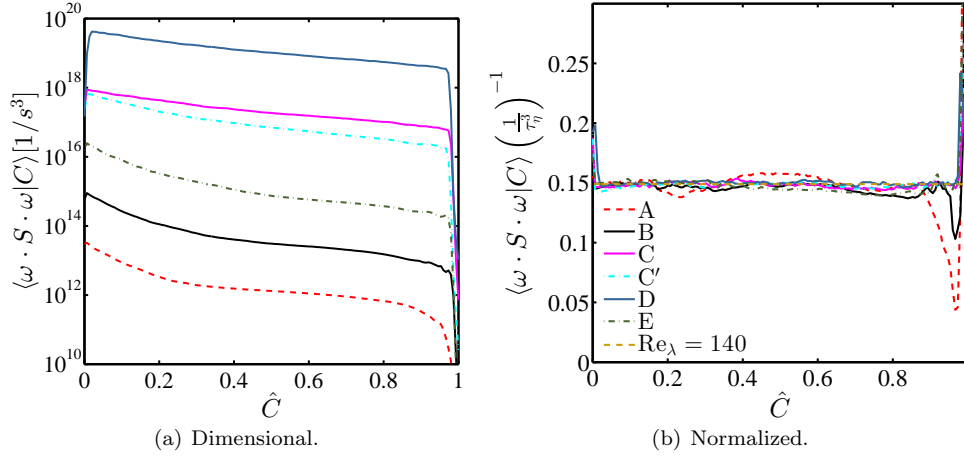
Fig. 20. Vortex stretching term in dimensional and normalized form. Oscillations at the smallest/largest values of $\hat{C}$ are due to the region where turbulence forcing is inactive. The line Re_λ is calculated from the previous simulations of homogeneous, isotropic turbulence by[44].

9.3. Baroclinic torque

Baroclinic torque, like dilatation, is only present due to the density variations within the flame. Likewise, it tends toward zero in the reactants and products. The following scaling for baroclinic torque is proposed,

$$\frac{\boldsymbol{\omega}}{\rho^2} \cdot (\nabla\rho \times \nabla P) \propto \gamma \frac{u_\eta}{l_F \tau_\eta^2}. \tag{55}$$

When normalized according to the above expression, the variation in the peak value between the six cases reduces from five orders of magnitude to a factor of 2.

9.4. Viscous dissipation

Viscous dissipation, like vortex stretching, is present in constant density flow. As with several quantities discussed prior, in the case of high Ka, viscous dissipation scales with the turbulent quantities, specifically,

$$\boldsymbol{\omega} \cdot \nabla \times \left(\frac{1}{\rho}\nabla \cdot \tau\right) \propto \frac{1}{\tau_\eta^3}. \tag{56}$$

In the the high Reynolds number limit of homogeneous, isotropic turbulence,[71] propose a similar scaling.

9.5. Normalized enstrophy transport equation

The above scaling estimates are used to propose a normalization of the entire enstrophy transport equation, which is then given by,

$$\frac{1}{2}\frac{D\hat{\omega}^2}{D\hat{t}} = Ka\hat{T}_1 + \gamma\hat{T}_2 + \alpha\gamma\sqrt{Ka}\hat{T}_3 + Ka\hat{T}_4 + \frac{1}{2Da}\hat{T}_5, \tag{57}$$

where, $\hat{t} = t/\tau_F$, $\hat{\omega}^2 = \langle\omega^2|C\rangle\tau_\eta^2$, and the Damköhler number is $Da = \tau_o/\tau_F$. As written above, $\hat{T}_1$ is vortex stretching, $\hat{T}_2$ is dilatation, $\hat{T}_3$ is baroclinic torque, $\hat{T}_4$ is viscous dissipation, and $\hat{T}_5$ is the forcing with each component normalized according to the above discussion. The preceding analysis in this section shows that the normalized terms obtain nearly constant values (or a constant peak value) through the flame and across conditions with $\hat{T}_1 \simeq 0.15$, $0 < \hat{T}_2 \lesssim 0.7$, $0 < \hat{T}_3 \lesssim 0.1$, $-0.25 < \hat{T}_4 < -0.15$, and $\hat{T}_5 \simeq 1$, at high Ka_u. The scaling in Eq. 57 suggests that as the Karlovitz number increases, vortex stretching and dissipation increase in magnitude relative to baroclinic torque, dilatation, and forcing. This explains the observed relative decrease of baroclinic torque and dilatation as Ka increased in the results of Hamlington et $al.$ [72].
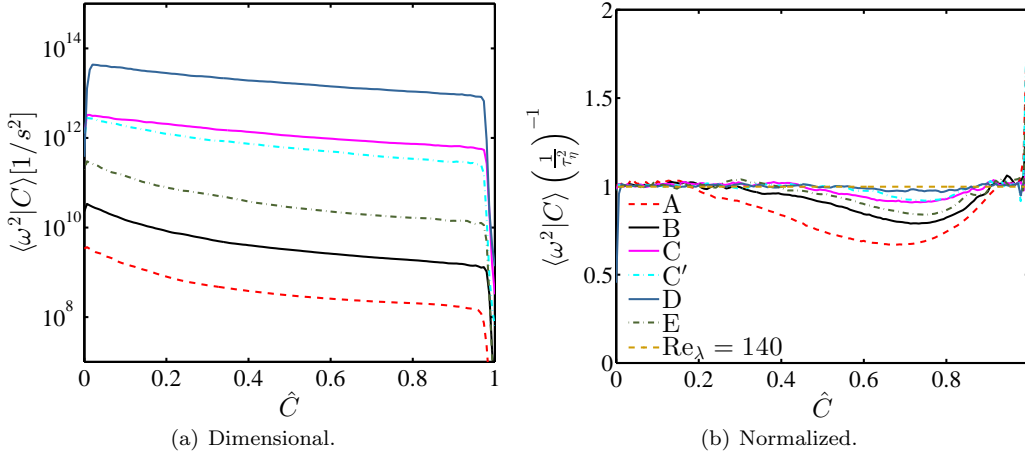
21

Fig. 21. Enstrophy in dimensional and normalized form. In normalized form, enstrophy has less variation through the flame as the Karlovitz number increases. The line Re_λ is calculated from the previous simulations of homogeneous, isotropic turbulence by[44].

9.6. *Kolomogorov's first hypothesis*

In the limit of high Ka, enstrophy transport results in a local balance between production and dissipation. This is also the case for homogeneous, isotropic turbulence[73,71]. This implies that enstrophy should scale with the Kolmogorov time scale, which is confirmed in Fig. 21, with a proportionality constant close to unity. From homogeneous, isotropic turbulence it can be shown that

$$\overline{\omega^2} = 15\overline{\left(\frac{\partial u}{\partial x}\right)^2},$$ (58)

so that a normalized value of unity is expected [67]. This demonstrates that it is the change in kinematic viscosity, as opposed to the effect of the density change through dilatation and baroclinic torque, which drives the enstrophy transformation through the flame.

These results shed light on the validity of Kolmogorov's first similarity hypothesis within premixed flames, since enstrophy is characteristic of the smallest turbulent scales. Though the fluid properties and turbulence characteristics vary widely across the flame and between the present cases, enstrophy is found to vary only as a function of τ_η, or equivalently ν and ϵ alone. This supports that Kolmogorov's first similarity hypothesis is valid for sufficiently high Karlovitz number premixed flames.

10. Impact of models and assumptions on turbulence evolution

The above conclusions are obtained using finite-rate chemistry and non-unity Lewis numbers. Turbulent combustion research often employs other chemical and transport models.

10.1. *Effects of unity-Lewis number assumption*

To test the effects of transport models, case B is repeated setting all Lewis numbers to unity, referred to as B_1. Figure 22a and b show that varying the transport model has negligible effects on the dimensional and normalized mean enstrophy. As vortex stretching and viscous dissipation dominate the transport of enstrophy at high Karlovitz number, the mean enstrophy evolves similarly in the two cases. It is important to note that this analysis is in the absence of thermo-diffusive instabilities, and these results may not extend to flames, such as lean hydrogen/air, where these instabilities occur.

10.2. *Effect of chemical models*

To investigate the implications of chemical models, case B_1 is repeated using two alternative chemical mechanisms: one-step ($B_{OS,1}$) and tabulated chemistry ($B_{Tab,1}$). In order to focus on the effects of the chemical model, unity Lewis numbers are used in all three simulations in order to eliminate effects due differences in the transport models.

The results obtained with each model are compared primarily through the mean enstrophy. Figure 23a and b shows that the chemical models induce little differences in the dimensional and normalized mean enstrophy. The agreement observed in the mean enstrophy further emphasizes that the smallest turbulent scales evolve through the flame with the local fluid properties, independent of the tested transport or chemical models.
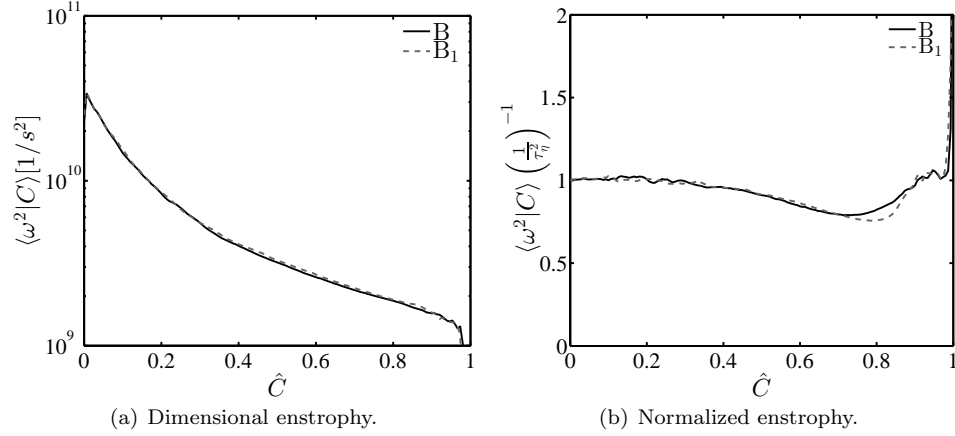
22

(a) Dimensional enstrophy.

(b) Normalized enstrophy.

Fig. 22. Comparison of case B with constant non-unity(B) and unity Lewis numbers(B_1).

(a) Dimensional enstrophy.
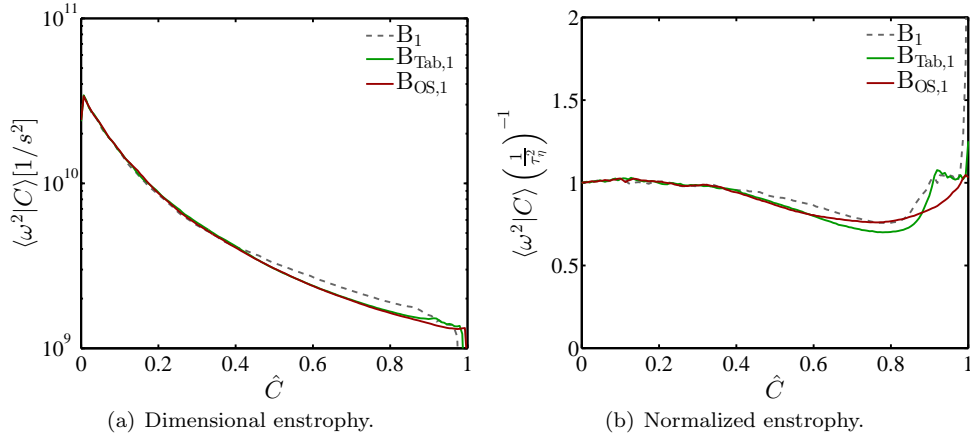
(b) Normalized enstrophy.

Fig. 23. Comparison of case B_1 with finite-rate, tabulated, and one-step chemistry.

10.3. *Extension to larger Reynolds numbers*

While this study considers a wide range of Karlovitz numbers, the integral length scale in each DNS discussed thus far is limited to approximately the flame thickness. It is important to consider whether these results are applicable to larger values of l_o/l_F, or equivalently, larger Reynolds numbers.

The portion of enstrophy contained in scales smaller than the flame thickness may be determined by considering the model spectrum of Pope for the high Re limit[67],

$$E(\kappa) = 1.5\epsilon^{2/3}\kappa^{-5/3}\left(\frac{\kappa l_o}{[(\kappa l_o)^2 + 6.78]^{1/2}}\right)^{11/3}\exp\left[-5.2\left([(\kappa\eta)^4 + 0.4^4]^{1/4} - 0.4\right)\right], \qquad (59)$$

and evaluating the vorticity spectrum as $\Omega(\kappa) = 2\kappa^2 E(\kappa)$. Considering an infinite Re, at least 80% of the enstrophy is contained in scales smaller than the flame if $l_F/\eta > 40$. This is approximately the condition of case B. Said otherwise, if case B had an arbitrarily large Re but the same Ka_u, then only 20% of the enstrophy would be in scales larger than the flame thickness. In summary, any high Reynolds number turbulent flame with the same Karlovitz number of the present cases would have nearly the same fraction of vorticity contained in scales smaller than the flame. The present results should thus remain valid for larger integral to flame length scale ratios.

An additional DNS, labeled case $B_{\mathrm{Tab},1}^4$, is performed to verify if the results are indeed independent of the Reynolds number. This simulation has the exact same conditions as case $B_{\mathrm{Tab},1}$, but a higher Reynolds number, $Re_t = 1150$. The increase in Re_t is accomplished by increasing both L as well as u', in order to maintain the same Ka_u number, resulting in a four-fold increase in the integral length scale ($l_o/l_F = 4$ and $u'/S_L = 33$). Figure 24 presents instantaneous density contour plots from $B_{\mathrm{Tab},1}$ and $B_{\mathrm{Tab},1}^4$. Figure 25 shows that increasing the turbulent Reynolds number introduces only small changes to these quantities.

(a) case $B_{\text{Tab},1}$
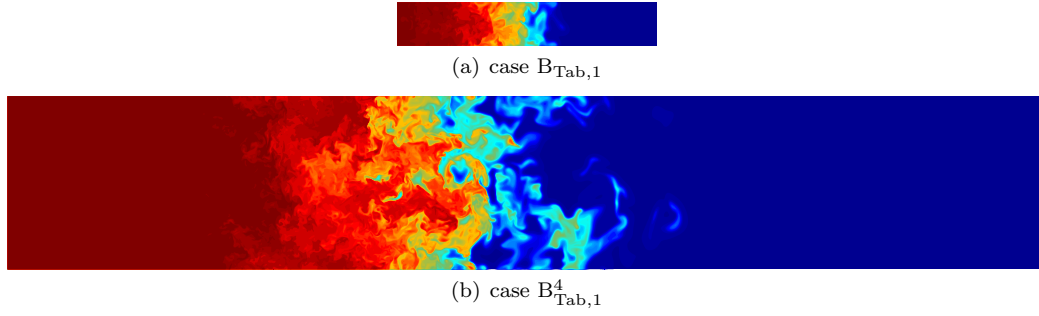

(b) case $B^4_{\text{Tab},1}$

Fig. 24. Two-dimensional slices of density from cases $B_{\text{Tab},1}$ and $B^4_{\text{Tab},1}$. Each figure represents a region of size $L \times 6L$ and both are scaled to match physical length scales.
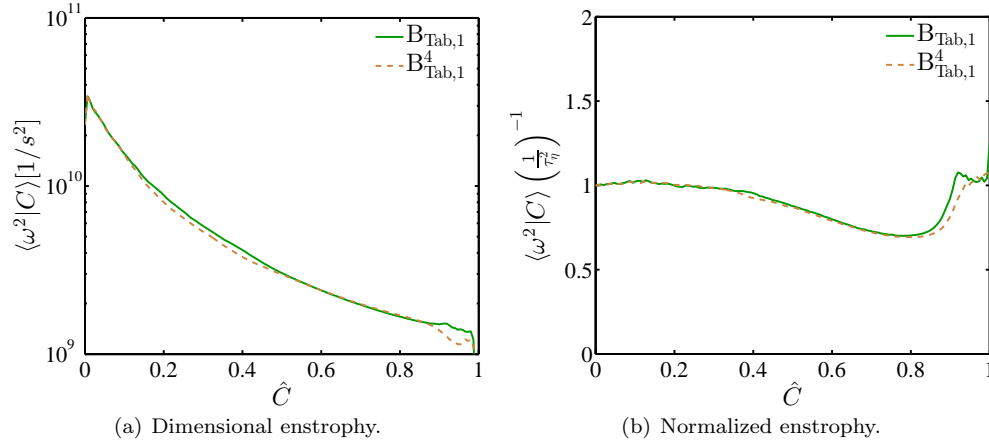

(a) Dimensional enstrophy.

(b) Normalized enstrophy.

Fig. 25. Comparison of case $B_{\text{Tab},1}$ with the case of a larger Reynolds number, $B^4_{\text{Tab},1}$.

References

[1] N. Peters, Turbulent Combustion, Cambridge University Press, Cambridge, 2000.

[2] H. Pitsch, Large-eddy simulation of turbulent combustion, Ann. Rev. Fluid Mech. 38 (2006) 453–482.

[3] Y. Chen, R. Bilger, Experimental investigation of three-dimensional flame-front structure in premixed turbulent combustion - II. Lean hydrogen/air Bunsen flames, Combust. Flame 138 (2004) 155–174.

[4] J. Hult, S. Gashi, N. Chakraborty, M. Klein, K. Jenkins, S. Cant, C. Kaminski, Measurement of flame surface density for turbulent premixed flames using PLIF and DNS, Proc. Comb. Inst. 31 (2007) 1319–1326.

[5] A. Aspden, M. Day, J. Bell, Turbulence-flame interactions in lean premixed hydrogen: transition to the distributed burning regime, J. Fluid Mech. 680 (2011) 287–320.

[6] A. Aspden, M. Day, J. Bell, Lewis number effects in distributed flames, Proc. Comb. Inst. 33 (2011) 1473–1480.

[7] R. Sankaran, E. Hawkes, J. Chen, T. Lu, C. Law, Structure of a spatially developing turbulent lean methane-air bunsen flame, Proc. Comb. Inst. 31 (2007) 1291–1298.

[8] W. Wang, K. Luo, J. Fan, Direct numerical simulation and conditional statistics of hydrogen/air turbulent premixed flames, Energ. Fuel 27 (2013) 549–560.

[9] E. Hawkes, O. Chatakonda, H. Kolla, A. Kerstein, J. Chen, A petascale direct numerical simulation study of the modelling of flame wrinkling for large-eddy simulations in intense turbulence, Combust. Flame 159 (2012) 2690–2703.

[10] A. Aspden, M. Day, J. Bell, Turbulence-chemistry interaction in lean premixed hydrogen combustion, Proc. Comb. Inst. 35 (2) (2015) 1321–1329.

[11] R. Cheng, D. Littlejohn, P. Strakey, T. Sidwell, Laboratory investigations of low-swirl injectors with H_2 and CH_4 at gas turbine conditions, Proc. Comb. Inst. 32 (2009) 3001–3009.

[12] M. Colket, T. Edwards, S. Williams, N. Cernansky, D. Miller, F. Egolfopoulos, P. Lindstedt, K. Seshadri, F. Dryer, C. Law, D. Friend, D. Lenhert, H. Pitsch, A. Sarofim, M. Smooke, W. Tsang, "Development of an experimental database and kinetic models for surrogate jet fuels" in 45th AIAA Aerospace Sciences Meeting and Exhibit (Reno, Nevada) (Jan. 8-11 2007).

[13] M. Mehl, W. J. Pitz, C. K. Westbrook, H. J. Curran, Kinetic modeling of gasoline surrogate components and mixtures under engine conditions , Proc. Comb. Inst. 33 (2011) 193 – 200.

[14] P. Curran, H.J. Gaffuri, W. Pitz, C. Westbrook, A comprehensive modeling study of n-heptane oxidation, Combust. Flame 114 (1998) 149–177.

[15] K. Niemeyer, C. Sung, Mechanism reduction for multicomponent surrogates: A case study using toluene reference fuels, Combust. Flame 161 (11) (2014) 2752–2764.

24

[16] P. Dagaut, M. Cathonnet, The ignition, oxidation, and combustion of kerosene: A review of experimental and kinetic modeling, Prog. Energy Combust. Sci. 32 (2006) 48–92.

[17] O. Desjardins, G. Blanquart, G. Balarac, H. Pitsch, High order conservative finite difference scheme for variable density low Mach number turbulent flows, J. Comput. Phys. 227 (15) (2008) 7125–7159.

[18] L. Shunn, F. Ham, P. Moin, Verification of variable-density flow solvers using manufactured solutions, J. Comput. Phys. 231 (9) (2012) 3801–3827.

[19] F. A. Williams, Combustion Theory 2nd Edition, Addison-Wesley, 1985.

[20] H. N. Najm, P. S. Wyckoff, O. M. Knio, A semi-implicit numerical scheme for reacting flow: I. Stiff chemistry, J. Comput. Phys. 143 (2) (1998) 381–402.

[21] O. M. Knio, H. N. Najm, P. S. Wyckoff, A semi-implicit numerical scheme for reacting flow: II. Stiff, operator-split formulation, J. Comput. Phys. 154 (2) (1999) 428–467.

[22] S. Dworkin, M. Smooke, V. Giovangigli, The impact of detailed multicomponent transport and thermal diffusion effects on soot formation in ethylene/air flames, Proc. Comb. Inst. 32 (1) (2009) 1165–1172.

[23] Y. Xuan, G. Blanquart, Numerical modeling of sooting tendencies in a laminar co-flow diffusion flame, Combust. Flame 160 (9) (2013) 1657–1666.

[24] Y. Xuan, G. Blanquart, Effects of aromatic chemistry-turbulence interactions on soot formation in a turbulent non-premixed flame, Proc. Comb. Inst. 35 (2) (2015) 1911–1919.

[25] Y. Xuan, G. Blanquart, M. E. Mueller, Modeling curvature effects in diffusion flames using a laminar flamelet model, Combust. Flame 161 (5) (2014) 1294–1309.

[26] P. Carroll, G. Blanquart, A proposed modification to Lundgren's physical space velocity forcing method for isotropic turbulence, Phys. Fluids 25 (2013) 105114.

[27] S. Verma, Y. Xuan, G. Blanquart, An improved bounded semi-Lagrangian scheme for the turbulent transport of passive scalars, J. Comput. Phys. 272 (0) (2014) 1 – 22.

[28] M. E. Mueller, H. Pitsch, LES model for sooting turbulent nonpremixed flames, Combust. Flame 159 (6) (2012) 2166–2180.

[29] F. Bisetti, G. Blanquart, M. Mueller, H. Pitsch, On the formation and early evolution of soot in turbulent nonpremixed flames, Combust. Flame 159 (2012) 317–335.

[30] P. Carroll, G. Blanquart, The effect of velocity field forcing techniques on the Karman-Howarth equation, J. Turbul. 15 (2014) 429–448.

[31] M. Herrmann, G. Blanquart, V. Raman, Flux corrected finite volume scheme for preserving scalar boundedness in reacting large–eddy simulations, AIAA Journal 44 (12) (2006) 2879–2886.

[32] C. D. Pierce, Progress-variable approach for large-eddy simulation of turbulent combustion, Ph.D. thesis, Stanford University (2001).

[33] L. F. Richardson, The approximate arithmetical solution by finite differences of physical problems involving differential equations, with an application to the stresses in a masonry dam, Philos. Trans. R. Soc. Lond. A 210 (1911) 307–357.

[34] F. Perini, E. Galligani, R. D. Reitz, A study of direct and Krylov iterative sparse solver techniques to approach linear scaling of the integration of chemical kinetics with detailed combustion mechanisms, Combust. Flame 161 (5) 1180–1195.

[35] Z. Hong, D. Davidson, R. Hanson, An improved H-2/O-2 mechanism based on recent shock tube/laser absorption measurements, Combust. Flame 158 (4) (2011) 633–644.

[36] G. P. Smith, D. M. Golden, M. Frenklach, N. W. Moriarty, B. Eiteneer, M. Goldenberg, C. T. Bowman, R. K. Hanson, S. Song, W. C. Gardiner, V. V. Lissianski, Z. Qin, GRI-Mech 3.0. Available at http://www.me.berkeley.edu/gri_mech/.

[37] G. Blanquart, CaltechMech v2.1. Available at http://theforce.caltech.edu/resources/.

[38] B. Savard, B. Bobbitt, G. Blanquart, Structure of a High Karlovitz n-C7H16 Premixed Turbulent Flame, Proc. Comb. Inst. 35 (2) (2015) 1377–1384.

[39] A. Poludnenko, E. Oran, The interaction of high-speed turbulence with flames: Global properties and internal flame structure, Combust. Flame 157 (2010) 995–1011.

[40] T. Lundgren, "Linear forced isotropic turbulence" in Annual Research Briefs (Center for Turbulence Research, Stanford) (2003) 461-473.

[41] C. Rosales, C. Meneveau, Linear forcing in numerical simulations of isotropic turbulence: Physical space implementations and convergence properties, Phys. Fluids 17 (2005) 095106.

[42] L. Mydlarski, Z. Warhaft, On the onset of high-Reynolds-number grid-generated wind tunnel turbulence, J. Fluid Mech. 320 (1996) 331–368.

[43] S. K. Lele, Compressibility effects on turbulence, Ann. Rev. Fluid Mech. 26 (1994) 211 – 254.

[44] P. L. Carroll, G. Blanquart, A proposed modification to Lundgren's physical space velocity forcing method for isotropic turbulence, Phys. Fluids 25 (2013) (105114).

[45] J. van Oijen, F. Lammers, L. de Goey, Modeling of complex premixed burner systems by using flamelet-generated manifolds, Combust. Flame 127 (2001) 2124–2134.

[46] O. Gicquel, N. Darabiha, D. Thévenin, Laminar premixed hydrogen/air counterflow flame simulations using flame prolongation of ILDM with differential diffusion, Proc. Comb. Inst. 28 (2000) 1901–1908.

[47] E. Knudsen, H. Pitsch, A general flamelet transformation useful for distinguishing between premixed and non-premixed modes of combustion, Combust. Flame 156 (2009) 678–696.

[48] S. Viswanathan, H. Wang, S. Pope, Numerical implementation of mixing and molecular transport in LES/PDF studies of turbulent reacting flows, J. Comp. Phys. 230 (2011) 6916–6957.

[49] S. Pope, Turbulent Flows, Cambridge University Press, Cambridge, 2000.

[50] E. Hawkes, J. Chen, Comparison of direct numerical simulation of lean premixed methane-air flames with strained laminar flame calculations, Combust. Flame 144 (2006) 112–125.

[51] N. Chakraborty, E. Hawkes, J. Chen, R. Cant, The effects of strain rate and curvature on surface density function in turbulent premixed methane-air and hydrogen-air flames: a comparative study, Combust. Flame 154 (2008) 259–280.

25

[52] D. Haworth, T. Poinsot, Numerical simulations of Lewis number effects in turbulent premixed flames, J. Fluid Mech. 244 (1992) 405–436.

[53] N. Chakraborty, R. Cant, Unsteady effects of strain rate and curvature on turbulent premixed flames in an inflow-outflow configuration, Combust. Flame 137 (2004) 129–147.

[54] H. Im, J. Chen, Preferential diffusion effects on the burning rate of interacting turbulent premixed hydrogen-air flames, Combust. Flame 131 (2002) 246–258.

[55] A. Kelly, A. Smallbone, D. Zhu, C. Law, Laminar flame speeds of C_5 to C_8 n-alkanes at elevated pressures and temperatures, in: 48th AIAA Aerospace Sciences Meeting, Orlando, USA, 2010.

[56] P. Yeung, S. Girimaji, S. Pope, Straining and scalar dissipation on material-surfaces in turbulence - implications for flamelets, Combust. Flame 79 (1990) 340–365.

[57] P. Venkateswaran, A. Marshall, D. Shin, D. Noble, Measurements and analysis of turbulent consumption speeds of H_2/CO mixtures, Combust. Flame 158 (2011) 1602–1614.

[58] H. Kobayashi, Y. Kawabata, K. Maruta, Experimental study on general correlation of turbulent burning velocity at high pressure, Proc. Comb. Inst. 27 (1998) 941–948.

[59] T. Kitagawa, T. Nakahara, K. Maruyama, K. Kado, A. Hayakawa, S. Kobayashi, Turbulent burning velocity of hydrogen-air premixed propagating flames at elevated pressures, Int. J. Hydrogen Energy 33 (2008) 5842–5849.

[60] H. Kobayashi, Y. Otawara, J. Wang, F. Matsuno, Y. Ogami, M. Okuyama, T. Kudo, S. Kadowaki, Turbulent premixed flame characteristics of a $CO/H_2/O_2$ mixture highly diluted with CO_2 in a high-pressure environment, Proc. Comb. Inst. 34 (2013) 1437–1445.

[61] S. Daniele, J. Mantzaras, P. Jansohn, A. Denisov, K. Boulouchos, Flame front/turbulence interaction for syngas fuels in the thin reaction zones regime: turbulent and stretched laminar flame speeds at elevated pressures and temperatures, J. Fluid Mech. 724 (2013) 36–68.

[62] F. Halter, C. Chauveau, I. Gökalp, Characterization of the effects of hydrogen addition in premixed methane/air flames, Int. J. Hydrogen Energy 32 (2007) 2585–2592.

[63] D. Bradley, A. Lau, M. Lawes, Flame stretch rate as a determinant of turbulent burning velocity, Phil. Trans. R. Soc. Lond. 338 (1992) 359–387.

[64] S. Muppala, M. Papalexandris, B. Manickam, K. Aluri, N, F. Dinkelacker, Numerical simulation of lean premixed turbulent hydrogen/hydrocarbon flames at elevated pressures, in: 10th International Workshop on Premixed Turbulent Flames, Mainz, Germany, 2006.

[65] G. Damkhöler, Der einfluss der turbulenz auf die flammengeschwindigkeit, Z. Elektrochem. 46 (1940) 601–652.

[66] T. Echekki, J. Chen, Unsteady strain rate and curvature effects in turbulent premixed methane-air flames, Combust. Flame 106 (1996) 184–202.

[67] S. B. Pope, Turbulent Flows, Cambridge University Press, 2000.

[68] C. Poulain, N. Mazellier, P. Gervais, Y. Gagne, C. Baudet, Spectral Vorticity and Lagrangian Velocity Measurements in Turbulent Jets, Flow, Turbul. Combust. 72 (2-4) (2004) 245–271.

[69] J. Jiménez, A. A. Wray, P. G. Saffman, R. S. Rogallo, The structure of intense vorticity in isotropic turbulence, J. Fluid Mech. 255 (1993) 65–90.

[70] S. C. Morris, J. F. Foss, Vorticity spectra in high Reynolds number anisotropic turbulence, Phys. Fluids 17 (8).

[71] H. Tennekes, J. L. Lumley, A first course in turbulence, MIT Press, 1972.

[72] P. E. Hamlington, A. Y. Poludnenko, E. S. Oran, Interactions between turbulence and flames in premixed reacting flows, Phys. Fluids 23 (12).

[73] G. I. Taylor, Production and Dissipation of Vorticity in a Turbulent Fluid, Proc. R. Soc. Lon. Ser.-A 164 (916) (1938) 15– 23. URL http://www.jstor.org/stable/96995

1.

1. Report Type

Final Report

Primary Contact E-mail
Contact email if there is a problem with the report.

g.blanquart@caltech.edu

Primary Contact Phone Number
Contact phone number if there is a problem with the report

626-395-4306

Organization / Institution name

California Institute of Technology

Grant/Contract Title
The full title of the funded effort.

Assessing Model Assumptions for Turbulent Premixed Combustion at High Karlovitz Number

Grant/Contract Number
AFOSR assigned control number. It must begin with "FA9550" or "F49620" or "FA2386".

FA9550-12-1-0144

Principal Investigator Name
The full name of the principal investigator on the grant or contract.

Guillaume Blanquart

Program Manager
The AFOSR Program Manager currently assigned to the award

Chiping Li

Reporting Period Start Date

06/01/2012

Reporting Period End Date

05/31/2015

Abstract

N-heptane/air premixed turbulent flames in the high-Karlovitz portion of the thin reaction zone regime are characterized and modeled using Direct Numerical Simulations (DNS) with detailed chemistry. To enable the present numerical study, a new time-integration scheme has been proposed for the simulation of stiff reacting flows. Using this scheme, a series of direct numerical simulations of high Karlovitz number, n-C_7H_{16}, turbulent premixed flames have been performed. It was found that the flame structure of these turbulent flames can be well captured by one-dimensional flames accounting for the effective species Lewis numbers. The reaction zone was found to remain thin, yet large fluctuations in the fuel burning rate were identified. Extinctions were observed only in the presence of differential diffusion, and these events were correlated with high curvature regions. A model to capture the burning fluctuations was proposed using a new flamelet approach. For the first time, the evolution of the turbulence (both turbulent kinetic energy and enstrophy) has been characterized through the flame. Under sufficiently high Karlovitz number, the first Kolmogorov's hypothesis has been confirmed. Finally, the impact of various chemical/transport model assumptions on the evolution of turbulence has been analysed.

Distribution Statement
This is block 12 on the SF298 form.

DISTRIBUTION A: Distribution approved for public release.

Distribution A - Approved for Public Release

Explanation for Distribution Statement

If this is not approved for public release, please provide a short explanation. E.g., contains proprietary information.

SF298 Form

Please attach your SF298 form. A blank SF298 can be found here. Please do not password protect or secure the PDF The maximum file size for an SF298 is 50MB.

AFOSR.TFP.pdf

Upload the Report Document. File must be a PDF. Please do not password protect or secure the PDF . The maximum file size for the Report Document is 50MB.

AFOSR_FinalReport.pdf

Upload a Report Document, if any. The maximum file size for the Report Document is 50MB.

Archival Publications (published) during reporting period:

Savard, B., Blanquart, G. An a priori model for the effective species Lewis numbers in premixed turbulent flames, Combustion and Flame (2014), 161, 1547-1557.

Savard, B., Brock, B., Blanquart, G. Structure of a High Karlovitz n-C7H16 Premixed Turbulent Flame, Proceedings of the Combustion Institute (2015), 35, 1377-1384.

Savard, B., Blanquart, G. Broken reaction zone and differential diffusion effects in high Karlovitz n-C7H16 premixed turbulent flames, Combustion and Flame (2015), 162, 2020-2033.

Savard, B., Xuan, Y. Bobbitt, B., Blanquart, G. A computationally-efficient, semi-implicit, iterative method for the time-integration of reacting flows with stiff chemistry, Journal of Computational Physics (2015), 295, 740-769.

Changes in research objectives (if any):

Change in AFOSR Program Manager, if any:

Extensions granted or milestones slipped, if any:

AFOSR LRIR Number

LRIR Title

Reporting Period

Laboratory Task Manager

Program Officer

Research Objectives

Technical Summary

Funding Summary by Cost Category (by FY, $K)

	Starting FY	FY+1	FY+2
Salary			
Equipment/Facilities			
Supplies			
Total			

Report Document

Report Document - Text Analysis

Report Document - Text Analysis

Appendix Documents

2. Thank You

E-mail user

Sep 02, 2015 13:50:35 Success: Email Sent to: g.blanquart@caltech.edu